Climate Sensitivity from 21st-Century Trends in Earth's Energy Imbalance

Vincent T. Cooper[1]

[1]Department of Earth, Atmospheric, and Planetary Sciences, Massachusetts Institute of Technology, Cambridge, MA, USA

Key Points:

- Energy-budget trends over 2006 to 2024 imply equilibrium climate sensitivity at the high end of but consistent with assessments of 2 to 5 K
- The trend-based constraint disfavors climate sensitivity below 2 K but provides little information about its upper bound
- Estimates of climate sensitivity depend strongly on the likelihood method; a revised method more directly follows the energy-balance model

Corresponding author: Vincent T. Cooper, vcooper@mit.edu

Abstract

Earth's energy imbalance has increased rapidly since continuous satellite observations began in 2001, raising concern that equilibrium climate sensitivity may be higher than in recent assessments. Here we use energy-budget trends over 2006–2024 to estimate climate sensitivity in a Bayesian framework, accounting for uncertainty in observations, forcing, variability, and pattern effects. Climate sensitivity inference depends strongly on the likelihood method, and we propose a simple, revised method that is physically consistent with the global energy-balance model. Its maximum likelihood is at 5.2 K, whereas the existing method maximizes at 3.0 K. Using the revised likelihood and a standard uniform-feedback prior, the posterior median is 3.6 K; posterior medians range from 3.3–4.8 K depending on the prior. Posterior 66% ranges largely overlap existing assessments of 2–5 K and strongly disfavor climate sensitivity below 2 K, but upper bounds are prior-dependent. Thus 21st-century trends do not require unusually high climate sensitivity compared to other lines of evidence.

Plain Language Summary

Earth is absorbing more energy than it releases to space, and satellite measurements show that this imbalance has grown rapidly since 2001. The trend in the imbalance is so large that it has raised concern that climate sensitivity—the long-term warming from a doubling of atmospheric CO_2—may be higher than recent assessments suggest. Combining satellite measurements of Earth's energy balance, estimates of anthropogenic and natural climate forcing, and observed global warming over 2006 to 2024 enables estimation of climate sensitivity, but the estimates depend strongly on the statistical framework. The revised statistical framework suggested in this study is more closely aligned with the physical model for climate sensitivity, and it finds that a climate sensitivity of 5.2 K best matches the recent data. However, after accounting for uncertainties and standard assumptions, the central estimate of climate sensitivity is 3.6 K (or 3.3 to 4.8 K with alternative assumptions). Climate sensitivity below 2 K appears unlikely, but the upper limit is not well informed by 21st-century trends. Overall, recent observations are compatible with existing assessments of roughly 2 to 5 K and do not require unusually high climate sensitivity.

1 Introduction

Earth's energy imbalance (EEI, typically denoted N) has increased rapidly since continuous satellite observations of Earth's top-of-atmosphere (TOA) radiation budget began in 2001 (Loeb et al., 2018, 2021; Raghuraman et al., 2021; Mauritsen et al., 2025; Allan & Merchant, 2025). Since 2001, the EEI trend has been nearly as large as the trend in effective radiative forcing (ERF), suggesting that Earth's radiative response to warming is only weakly stabilizing. Thus a key question is whether the weak stabilizing response implied by these trends also portends high climate sensitivity and extreme global warming (Stevens et al., 2026; Hansen et al., 2025; Goessling et al., 2025).

Earth's energy budget and climate sensitivity are commonly investigated using the standard global energy-balance model (Gregory et al., 2002):

$$N = F + R + \epsilon, \tag{1}$$

$$N = F + \lambda T + \epsilon, \tag{2}$$

where F is the effective radiative forcing, R is the radiative response to changing surface temperature, and ϵ is the stochastic contribution from internal variability. R is typically estimated as a radiative feedback (λ) multiplied by the change in surface air temperature (T). All quantities are global-mean anomalies from a reference state. Equilibrium climate sensitivity, $S = -F_{2\mathrm{xCO_2}} \,/\, \lambda_{2\mathrm{xCO_2}}$, is the steady-state warming following a doubling of CO_2 (Charney et al., 1979; Sherwood et al., 2020).

Stevens et al. (2026) show how trends in N, F, and T during the "Clouds and the Earth's Radiant Energy System" (CERES; Loeb et al., 2018) satellite era can be used to estimate a radiative feedback. Here, dot notation denotes the linear trend over the analysis period. Applying the linear-trend operator to each term in Eq. (1) yields

$$\dot{N} = \dot{F} + \dot{R} + \eta, \tag{3}$$

$$\dot{N} = \dot{F} + \lambda_{dt}\dot{T} + \eta, \tag{4}$$

where $\lambda_{dt} \equiv \dot{R} \,/\, \dot{T}$ is the feedback associated with the trends and is conceptually similar to the differential feedback (Tam et al., 2026; Ceppi et al., 2026b; Rugenstein & Armour, 2021; Ceppi & Gregory, 2019), while η is the stochastic contribution. With η set to its expected value of zero, the plug-in central estimate for λ_{dt} is $(\dot{N} - \dot{F}) \,/\, \dot{T}$. Because central estimates of $\dot{N}$ and $\dot{F}$ are quite similar over 2001–2024 while $\dot{T}$ is large, λ_{dt} appears to have a weak magnitude of -0.51 W m^{-2} K^{-1}. If λ_{dt} is an analog for $\lambda_{2\mathrm{xCO_2}}$ and

$F_{2\mathrm{xCO_2}} \approx 3.93\ \mathrm{W\,m^{-2}}$ (Forster et al., 2021), the plug-in estimate from these trends is a very high S of 7.7 K (Stevens et al., 2026).

To estimate $\lambda_{2\mathrm{xCO_2}}$ and S, we adapt existing approaches that account for pattern effects, i.e., differences between the diagnosed λ_{dt} and $\lambda_{2\mathrm{xCO_2}}$ due to differences in the pattern of warming (Armour et al., 2013; Andrews et al., 2015; Rugenstein et al., 2023). Including a pattern-effect adjustment, quantified as $\Delta\lambda = \lambda_{2\mathrm{xCO_2}} - \lambda_{dt}$ (Armour, 2017; Andrews et al., 2018, 2022; Sherwood et al., 2020; Forster et al., 2021), enables inference of $\lambda_{2\mathrm{xCO_2}}$ with the following equation:

$$\dot{N} = \dot{F} + (\lambda_{2\mathrm{xCO_2}} - \Delta\lambda)\,\dot{T} + \eta. \tag{5}$$

In this study, we merge the trend-based approach of Stevens et al. (2026) with the Bayesian framework of Sherwood et al. (2020), hereafter SW20, to produce estimates of $\lambda_{2\mathrm{xCO_2}}$ and S and their uncertainties using 21st-century trends in Earth's energy budget. Our main goals are 1) to examine whether estimates of $\lambda_{2\mathrm{xCO_2}}$ from recent trends are consistent with existing assessments of $\lambda_{2\mathrm{xCO_2}}$ and S, and 2) to show how constraints from the recent trends could be included in the Bayesian framework established by SW20.

2 21st-century Trends in Earth's Energy Budget

2.1 Sources of Data on N, F, T, and $\Delta\lambda$

CERES EBAF Ed4.2.1 (Loeb et al., 2018) provides global-mean N; the Indicators of Global Climate Change (IGCC; Forster et al., 2025; Smith et al., 2025) provide a 100,000-member ensemble of F by extending the methods of Forster et al. (2021); and HadCRUT5.1 (Morice et al., 2021) provides a 200-member ensemble of T. Results are similar using other estimates of T (e.g., Thorne et al., 2026; Chan et al., 2026; Cooper et al., 2025) due to the relatively small uncertainty in observations of T over the 21st century.

$\Delta\lambda$ is estimated using the simulations in atmospheric general circulation models (AGCMs) from Cooper et al. (2026a). The simulations have time-varying prescribed sea-surface temperature (SST) and sea ice concentration (SIC) with constant preindustrial forcings (Gregory & Andrews, 2016; Andrews, 2014), yielding $\lambda_{dt} = \dot{R}\,/\,\dot{T}$. $\Delta\lambda$ is then estimated as the difference between a coupled model's $\lambda_{2\mathrm{xCO_2}}$ (typically approximated using $\lambda_{4\mathrm{xCO_2}}$) and the diagnosed feedback in its corresponding AGCM (e.g., Andrews et al., 2018, 2022). The $\Delta\lambda$ estimates come from 62 simulations in six equally weighted

AGCMs with observational SST and sea ice from Cooper et al. (2025). The simulations end in 2023, and additional AGCMs and boundary conditions used in upcoming intercomparison projects could refine estimates of $\Delta\lambda$ for use in future studies (Schmidt et al., 2023; Ceppi et al., 2026a).

In the Supporting Information (SI), we include a test where the forcing trend in Forster et al. (2025) is increased by 0.15 $\mathrm{W\,m^{-2}\,dec^{-1}}$. This test is motivated by Van Loon et al. (2025) and quantitatively informed by Yuan et al. (2026)'s process-based estimates of the forcing from aerosol-cloud interactions (ERFaci). Yuan et al. (2026) suggest ERFaci trends over 2003–2023 are 0.33 $\mathrm{W\,m^{-2}\,dec^{-1}}$ over oceanic regions, which scales to a global estimate of 0.25 $\mathrm{W\,m^{-2}\,dec^{-1}}$ including Twomey effects over land. Using Yuan et al. (2026)'s results and the same scale factor of ($0.25/0.33 \approx 0.75$) produces an estimated ERFaci trend of 0.29 $\mathrm{W\,m^{-2}\,dec^{-1}}$ for 2006–2023, which exceeds IGCC's mean ERFaci trend by 0.15 $\mathrm{W\,m^{-2}\,dec^{-1}}$. We assume this trend difference for 2006–2023 would be approximately the same for 2006–2024, which is the period we use for our main inference of $\lambda_{2\mathrm{xCO_2}}$, as explained below.

2.2 Linear Trends and Uncertainties

Figure 1 shows time series and trend estimates for N, F, and T over 2001–2024 and 2006–2024. When using the λ_{dt} method to estimate feedbacks, curvature in the time series can make the inferred λ_{dt} sensitive to the selected period. In other words, estimates of λ_{dt} are expected to be more reliable for periods with sufficiently linear time series in N, F, and T. Curvature in F is identified as particularly important for 2001–2024: F decreases slightly over 2001–2006 before increasing linearly over 2006–2024, as shown in Fig. 1c and SI Fig. S1. The decrease between 2001 and 2006 is strongly influenced by aerosol forcing, which is also shown in Fig. 1c and has a mean change of -0.19 $\mathrm{W\,m^{-2}}$. Natural forcings from volcanism and insolation also decrease over this period. The root-mean squared error and mean absolute error of the linear fits for total F are both approximately twice as large for 2001–2024 as for 2006–2024. Since mid-2005, N from CERES has also been cross-checked against in situ oceanic observations from Argo (Loeb et al., 2021; Johnson et al., 2016; Hakuba et al., 2024). We therefore use 2006–2024 for our main analysis and retain 2001–2024 for comparison only. Relative to 2001–2024, changing the period to 2006–2024 shifts the plug-in estimate of λ_{dt} by -0.25 $\mathrm{W\,m^{-2}\,K^{-1}}$, from -0.51 to -0.76 $\mathrm{W\,m^{-2}\,K^{-1}}$, which still implies a high S of 5.2 K.

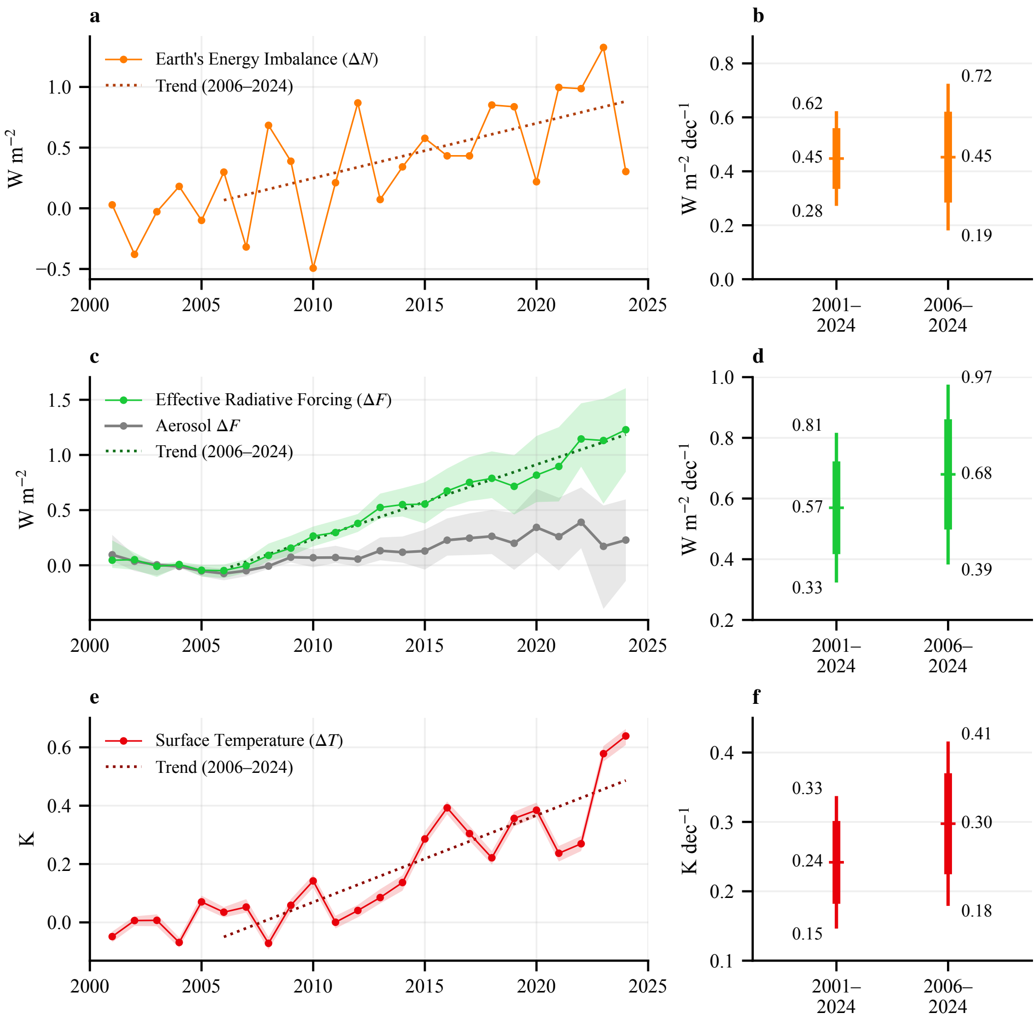

Figure 1. Time series for Earth's energy imbalance, effective radiative forcing, and surface temperature over 2001–2024, including estimates of forced trends and uncertainty. **(a)** Earth's energy imbalance (N) from CERES EBAF Ed4.2.1 and **(b)** estimates of forced trends in N for 2001–2024 and 2006–2024; horizontal lines show medians, thick bars show 66% intervals, and thin bars show 90% intervals. **(c–d)** Forcing time series and trends from the Forster et al. (2025) ensemble (shading is ensemble 90% range), including the time series for the anthropogenic-aerosol component of forcing. **(e–f)** Surface temperature from the HadCRUT5.1 ensemble (shading is ensemble 90% range). All time series show anomalies relative to their 2001–2006 means. Trend uncertainties for N and T account for internal variability.

CERES does not directly estimate the uncertainty in N, thus assessing the forced trend's uncertainty is nontrivial (Raghuraman et al., 2021; Loeb et al., 2022). CERES provides a central estimate of the time series, and from this we estimate $\dot{N}$ by applying ordinary least squares (OLS) regression to annual means. The resulting standard errors are approximately 10% larger than estimates using monthly means with an autocorrelation adjustment (Loeb et al., 2022). The OLS standard error reflects measurement noise and interannual variability insofar as they contribute to the regression residuals, but it could miss additional error from low-frequency internal variability. We test for such additional error variance using non-overlapping 19- and 24-year segments from preindustrial-control simulations of CESM2 (1200 years; Danabasoglu et al., 2020) and MPI-ESM1.2-LR (1000 years; Mauritsen et al., 2019). Each model's variance across trends is no larger than its mean-squared standard error from OLS regression within the segments, therefore we find no evidence of additional uncertainty in $\dot{N}$ beyond that represented by the OLS standard error. Raghuraman et al. (2021) similarly report that regression-based and model-derived estimates of internal-variability uncertainty are comparable in magnitude. Hence the OLS standard errors of $1\sigma = 0.10\ \mathrm{W\,m^{-2}\,dec^{-1}}$ for 2001–2024 and $0.16\ \mathrm{W\,m^{-2}\,dec^{-1}}$ for 2006–2024 are used here as the total uncertainty in $\dot{N}$ (Fig. 1b). The 2001–2024 value is similar to Chen et al. (2026)'s assessed value of $1\sigma = 0.11\ \mathrm{W\,m^{-2}\,dec^{-1}}$, which follows Raghuraman et al. (2021)'s methods. Given the consistency between $\dot{N}$ estimates using CERES versus ocean heat content (Loeb et al., 2021; Allan & Merchant, 2025), we do not add additional structural uncertainty. The preindustrial-control simulations also estimate covariance between $\dot{N}$ and $\dot{T}$, which is accounted for in the likelihood calculations in Section 3. The assumed distributions for $\dot{N}$ and the other parameters are summarized in SI Table S1.

Uncertainty estimates for $\dot{F}$ (Fig. 1c–d) are available from IGCC's 100,000-member ensemble, although the IGCC ensemble does not necessarily include all components of structural uncertainty. The variance in trends across the ensemble provides an initial uncertainty estimate, but recent studies suggest that the uncertainty in ERFaci may be underestimated (Van Loon et al., 2025; Yuan et al., 2026; Ceppi et al., 2026b; Park & Soden, 2025; Hodnebrog et al., 2024). Based on the differences between the central estimates of ERFaci trends in IGCC versus Yuan et al. (2026) and Park and Soden (2025), we add an additional error of $0.1\ \mathrm{W\,m^{-2}\,dec^{-1}}$ in quadrature to account for structural uncertainty. This error comprises approximately 30% of the total variance in $\dot{F}$ over 2006–2024.

Uncertainty in $\dot{T}$ (Fig. 1e–f) across the 200-member HadCRUT5.1 ensemble is small because all ensemble members represent the same realized climate history. The ensemble spread represents the small observational uncertainty but does not sample the uncertainty in the forced trend arising from internal variability. This component is estimated as the mean variance across non-overlapping trends in the CESM2 and MPI-ESM1.2-LR preindustrial-control simulations, as described above for $\dot{N}$. The internal-variability variance is then added to the HadCRUT5.1 ensemble variance, and internal variability accounts for more than 95% of the total error variance in $\dot{T}$.

$\Delta\lambda$ is a key piece of Eq. (5) that is not available in observations alone and requires model-based estimates. The AGCM simulations in Cooper et al. (2026a) show that estimates of $\Delta\lambda$ depend on the period: equal-weighted multi-model means of $\Delta\lambda$ range from -0.09 to $0.51\ \mathrm{W\,m^{-2}\,K^{-1}}$ as the start year varies from 2001–2006 and the end year from 2019–2023. The simulations sample 14 plausible SST/SIC patterns in four AGCMs, while three of the patterns are prescribed in all six AGCMs. These two subsets are used to estimate variance associated with AGCM physics, SST/SIC uncertainty, model-dependent responses to the SST/SIC patterns, and atmospheric variability from initial conditions. Differences across AGCMs and their pattern-dependent responses are the largest contribution, accounting for approximately 65–75% of the total variance. SST/SIC uncertainty accounts for approximately 8–17%, which is also examined in Fan et al. (2025), while atmospheric variability accounts for approximately 18%. The total assessed uncertainty in $\Delta\lambda$ is approximately $0.3\ \mathrm{W\,m^{-2}\,K^{-1}}$ (SI Text S1). The mean estimate is $-0.03\ \mathrm{W\,m^{-2}\,K^{-1}}$ for 2006–2023 and $0.09\ \mathrm{W\,m^{-2}\,K^{-1}}$ for 2001–2023, but considering the large year-to-year noise, lack of a clear expectation for the sign of $\Delta\lambda$, and small sample of AGCMs, the central estimate of $\Delta\lambda$ is assumed to be zero. This trend-based result for $\Delta\lambda$ is consistent with results based on the differential feedback over 2006–2023 in Cooper et al. (2026a), which found that the 2006–2023 differential feedback is similar to $\lambda_{2\mathrm{xCO_2}}$ estimated by corresponding coupled models. While the λ_{dt} and $\lambda_{2\mathrm{xCO_2}}$ feedbacks appear similar, the observed warming pattern for 2006–2023 still has substantial differences compared to the long-term warming patterns for $2\mathrm{xCO_2}$ projected by coupled models.

3 Inference of Climate Sensitivity

3.1 Likelihood Estimation

We estimate $\lambda_{2\mathrm{xCO_2}}$ and S using Bayes's theorem, e.g.,

$$p(\lambda_{2\mathrm{xCO_2}} \mid \mathbf{y}) = \frac{p(\mathbf{y} \mid \lambda_{2\mathrm{xCO_2}})\, p(\lambda_{2\mathrm{xCO_2}})}{p(\mathbf{y})}, \tag{6}$$

where $\mathbf{y} = (\dot{N}, \dot{T})$ contains the observed trends, $p(\lambda_{2\mathrm{xCO_2}} \mid \mathbf{y})$ is the posterior, $\mathcal{L} = p(\mathbf{y} \mid \lambda_{2\mathrm{xCO_2}})$ is the likelihood, $p(\lambda_{2\mathrm{xCO_2}})$ is the prior, and $p(\mathbf{y})$ is a normalization factor. The likelihood $\mathcal{L}$ measures how compatible the observed trends are with each proposed value of $\lambda_{2\mathrm{xCO_2}}$ or S, after accounting for uncertainty in the observations and "nuisance parameters," such as $\dot{F}$, $\Delta\lambda$, and $F_{2\mathrm{xCO_2}}$ (Gelman et al., 2013). When inferring S, we assume $F_{2\mathrm{xCO_2}}$ is normally distributed with mean 3.93 $\mathrm{W\,m^{-2}}$ and standard deviation 0.29 $\mathrm{W\,m^{-2}}$ (Forster et al., 2021).

Importantly, the likelihood depends on the statistical model used to interpret the observations (Marvel & Webb, 2025; Gelman et al., 2017). The marginal likelihoods in SW20 are constructed using the T form of the energy budget:

$$\dot{T}_{\mathrm{pred}} = \frac{\dot{N} - \dot{F}}{\lambda_{2\mathrm{xCO_2}} - \Delta\lambda}, \qquad \dot{T}_{\mathrm{obs}} \sim \mathcal{N}\left(\dot{T}_{\mathrm{pred}}, \sigma^2_{\dot{T}}\right). \tag{7}$$

This likelihood, denoted $\mathcal{L}_T$, evaluates the probability density of the observed $\dot{T}$ given $\dot{T}_{\mathrm{pred}}$ and $\sigma^2_{\dot{T}}$. For a fixed value of $\lambda_{dt} = \lambda_{2\mathrm{xCO_2}} - \Delta\lambda$, and temporarily treating the errors as independent, marginalizing over uncertainty in $\dot{N}$ and $\dot{F}$ gives the effective variance of the residual $(\dot{T}_{\mathrm{obs}} - \dot{T}_{\mathrm{pred}})$,

$$V_T(\lambda_{dt}) = \sigma^2_{\dot{T}} + \frac{\sigma^2_{\dot{N}} + \sigma^2_{\dot{F}}}{\lambda^2_{dt}},$$

which increases as λ_{dt} approaches zero (SI Text S2).

Here, we propose instead using the energy-budget model of Eq. (5) in its native form,

$$\dot{N}_{\mathrm{pred}} = \dot{F} + (\lambda_{2\mathrm{xCO_2}} - \Delta\lambda)\dot{T}, \qquad \dot{N}_{\mathrm{obs}} \sim \mathcal{N}\left(\dot{N}_{\mathrm{pred}}, \sigma^2_{\dot{N}}\right). \tag{8}$$

This likelihood, denoted $\mathcal{L}_N$, evaluates the probability density of the observed $\dot{N}$ given $\dot{N}_{\mathrm{pred}}$ and $\sigma^2_{\dot{N}}$. For fixed λ_{dt} and independent errors, marginalizing over uncertainty in $\dot{T}$ and $\dot{F}$ gives the effective variance of the residual $(\dot{N}_{\mathrm{obs}} - \dot{N}_{\mathrm{pred}})$,

$$V_N(\lambda_{dt}) = \sigma^2_{\dot{N}} + \sigma^2_{\dot{F}} + \lambda^2_{dt}\sigma^2_{\dot{T}},$$

which remains finite as λ_{dt} approaches zero and increases with the magnitude of λ_{dt} (SI Text S2).

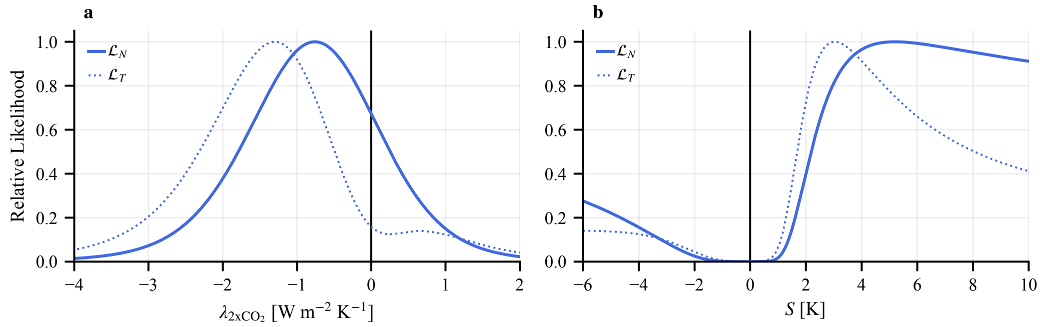

Figure 2. Likelihoods for the net radiative feedback (λ_{2xCO_2}) and climate sensitivity (S) based on trends over 2006–2024. (a) Likelihoods for λ_{2xCO_2} using two forms of the likelihood function: $\mathcal{L}_N$ from Eq. (8) and $\mathcal{L}_T$ from Eq. (7). **(b)** Likelihoods for $S = -F_{2xCO_2} / \lambda_{2xCO_2}$, as in panel **a**. Likelihoods are shown as relative likelihoods with a maximum of 1.0, i.e., all likelihood values are divided by the maximum value. Additional methods are compared in SI Fig. S2.

Although Eqs. (7) and (8) are algebraically equivalent, $\mathcal{L}_T$ and $\mathcal{L}_N$ are different statistical models because they evaluate Gaussian residual errors in different response variables. In $\mathcal{L}_T$, dividing the uncertain quantity $\dot{N} - \dot{F}$ by a near-zero feedback magnifies its uncertainty, causing $\mathcal{L}_T$ to down-weight high values of S and small magnitudes of λ_{2xCO_2}. With $\mathcal{L}_N$, uncertainties in $\dot{N}$ and $\dot{F}$ remain additive and are not divided by the proposed feedback, thus $\mathcal{L}_N$ does not a priori down-weight high S and small-magnitude λ_{2xCO_2}. The consequences are further explained below and in SI Text S2.

We evaluate both likelihoods by Monte Carlo integration over uncertainty in $\dot{N}$, $\dot{T}$, $\dot{F}$, and $\Delta\lambda$ (and F_{2xCO_2} when inferring $S = -F_{2xCO_2} / \lambda_{2xCO_2}$). Our full calculations also account for covariance between $\dot{N}$ and $\dot{T}$ (SI Text S3); the simplified expressions above are shown for clarity. We also show that the differences between $\mathcal{L}_N$ and $\mathcal{L}_T$ are not due to numerical issues with Monte Carlo integration, since the results are unchanged if the likelihoods are calculated analytically (SI Fig. S2).

The $\mathcal{L}_N$ likelihoods maximize at $\lambda_{2xCO_2} = -0.76$ W m^{-2} K^{-1} and $S = 5.2$ K (Fig. 2), as expected based on plug-in central estimates of the trends over 2006–2024. Corresponding values for 2001–2024 are $\lambda_{2xCO_2} = -0.51$ W m^{-2} K^{-1} and $S = 7.7$ K, which align with Stevens et al. (2026). On the other hand, $\mathcal{L}_T$ maximizes at -1.30 W m^{-2} K^{-1} and $S = 3.0$ K, and it is bimodal because its feedback-dependent weighting gives greater weight to larger magnitudes of λ_{dt} (SI Text S2). At $\lambda_{2\text{xCO}_2} = 0$, the relative likelihood (i.e., the ratio of $\mathcal{L}$ to its maximum value) of $\mathcal{L}_N$ is approximately 0.7 while $\mathcal{L}_T$'s is 0.2. Prior knowledge typically eliminates zero and positive values of $\lambda_{2\text{xCO}_2}$, but there are substantial differences between the two likelihoods even for negative values of $\lambda_{2\text{xCO}_2}$, indicating strong dependence on the choice of likelihood function.

The likelihood is not uniquely determined by the algebraic energy-budget equation; it follows from specifying a statistical model for the residual errors, so $\mathcal{L}_N$ and $\mathcal{L}_T$ correspond to different representations of data-generating model (Gelman et al., 2013, 2020). We prefer $\mathcal{L}_N$ because it most directly represents the physical energy-balance model of Eqs. (2) and (4) as a generative model, with the energy-budget residual η entering additively in N rather than being divided by λ_{dt} after rearrangement into T space (SI Text S2). Thus $\mathcal{L}_N$ remains well defined as λ_{dt} approaches zero.

However, $\mathcal{L}_N$ is not weight-free. Marginalizing over uncertainty in $\dot{T}$ in $\mathcal{L}_N$ implicitly adopts a uniform prior on the true temperature trend. Through the energy-budget Jacobian $d\dot{N} = |\lambda_{\text{dt}}|\, d\dot{T}$, there is an implicit prior of $1/|\lambda_{\text{dt}}|$ on the true $\dot{N}$, which mildly favors smaller feedback magnitudes and hence higher S (SI Text S2). $\mathcal{L}_T$ makes the opposite choice: a uniform prior on true $\dot{N}$ corresponds to a prior on true $\dot{T}$ that grows as $|\lambda_{\text{dt}}|$, which down-weights small feedback magnitudes. Preference for $\mathcal{L}_N$ rests on generative-model consistency rather than neutrality: η is defined as an additive energy-budget residual in Eq. (4), so its Gaussian distribution is naturally specified in N space, where its scale is independent of the proposed feedback. As a useful consistency check, $\mathcal{L}_N$'s maximum also coincides with the plug-in estimate, consistent with the linear-Gaussian limit (Fig. 2). Using $\mathcal{L}_N$ also addresses issues raised by Lewis (2023) regarding SW20's method of likelihood estimation.

We compare additional likelihood methods in SI Fig. S2. The profile likelihood considered by Lewis (2023) is nearly identical to $\mathcal{L}_N$ in this application, although profile and marginal likelihoods need not generally agree. The surface-integral method of Marvel and Webb (2025) produces a lower maximum-likelihood estimate of $S = 4.1$ K compared to $\mathcal{L}_N$ because, under its chosen coordinate scaling, its geometric weighting of $[(\lambda_{2\text{xCO}_2} - \Delta\lambda)^2 + 2]^{1/2}$ favors larger feedback magnitudes. For the remainder of our analysis, we use $\mathcal{L}_N$.

In summary, there are two key points based on the likelihoods alone: 1) The relative likelihood for $\mathcal{L}_N$ is greater than 0.7 for $\lambda_{2\mathrm{xCO_2}}$ between approximately -1.5 and 0.0 $\mathrm{W\,m^{-2}\,K^{-1}}$, indicating substantial overlap with existing estimates of $\lambda_{2\mathrm{xCO_2}}$ (e.g., Sherwood et al., 2020; Forster et al., 2021; Cooper et al., 2026a, 2026b; Zelinka et al., 2026); and 2) the likelihood depends strongly on the statistical model used to interpret the data, e.g., $\mathcal{L}_T$ versus $\mathcal{L}_N$. $\mathcal{L}_T$ has a much lower likelihood of high S compared to our preferred form, $\mathcal{L}_N$, which more directly represents the physical energy-balance model of Eq. (4) and the nature of its stochastic errors.

3.2 Prior Distributions

The prior typically has a substantial influence on the posterior, especially when estimating climate sensitivity from a single line of evidence (e.g., Frame et al., 2005; Pueyo, 2012; Lewis, 2014; Bodman & Jones, 2016). Figure 3 shows three plausible priors.

First, uniform λ is the baseline prior in SW20. Its posterior for $\lambda_{2\mathrm{xCO_2}}$ is proportional to the $\lambda_{2\mathrm{xCO_2}}$ likelihood. The prior does not eliminate positive values of $\lambda_{2\mathrm{xCO_2}}$, since we use prior support of $\lambda_{2\mathrm{xCO_2}} \in (-20, 10)$ $\mathrm{W\,m^{-2}\,K^{-1}}$, but we restrict the prior support to $S \in (0.05, 20)$ K when estimating S. Because the priors use different supports in $\lambda_{2\mathrm{xCO_2}}$ versus S space, their posteriors are not exact coordinate transformations of one another.

The second prior, a weakly informative choice (Gelman et al., 2008, 2017), is lognormal in $|\lambda_{2\mathrm{xCO_2}}|$ and nearly lognormal in S, with small departures arising from uncertainty in $F_{2\mathrm{xCO_2}}$. It maintains large uncertainty while enforcing broad physical constraints: $\lambda_{2\mathrm{xCO_2}}$ must be negative, and its probability density approaches zero both as $\lambda_{2\mathrm{xCO_2}} \to 0$ and as $\lambda_{2\mathrm{xCO_2}} \to -\infty$ (Goodwin & Cael, 2021; Goodwin, 2021). The prior distribution requires two parameters, the prior median and logarithmic standard deviation of $\lambda_{2\mathrm{xCO_2}}$, which we set to -1.0 $\mathrm{W\,m^{-2}\,K^{-1}}$ and 0.8, respectively, to place approximately 95% of the prior probability for S between 1–19 K without truncation. This choice is informed by a common truncation range of 0–20 K in previous studies, e.g., SW20. For $\lambda_{2\mathrm{xCO_2}}$, 95% of the prior probability is between -5 and -0.2 $\mathrm{W\,m^{-2}\,K^{-1}}$ without truncation.

The third prior is expert-informed and uses only the process-based assessment of feedbacks in SW20. SW20's process λ has a normal distribution in $\lambda_{2\mathrm{xCO_2}}$ with mean

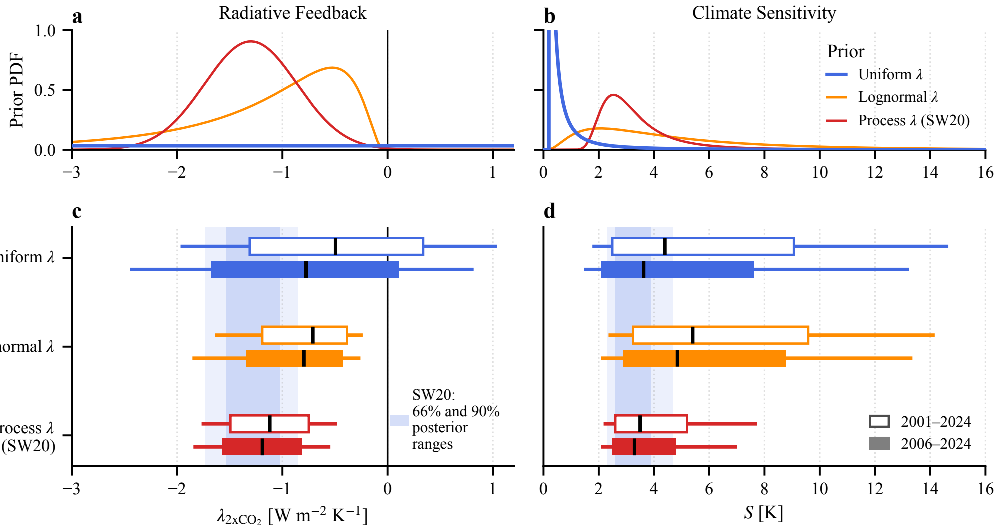

Figure 3. Prior probability density functions (PDFs) and posterior ranges for the radiative feedback ($\lambda_{2\text{xCO}_2}$) and climate sensitivity (S) based on CERES-era trends. **(a–b)** Three prior PDFs for $\lambda_{2\text{xCO}_2}$ and $S = -F_{2\text{xCO}_2}/\lambda_{2\text{xCO}_2}$; note that uniform λ is restricted to negative values when inferring S, i.e., the prior support for S is $(0.05, 20)$ K. **(c–d)** Posteriors corresponding to each prior, with medians shown by black lines and 66% and 90% ranges as thick and thin lines, respectively, for 2001–2024 and 2006–2024; posterior ranges from the baseline estimate in SW20 (Sherwood et al., 2020) are shown for comparison in blue shading.

-1.30 and standard deviation 0.44 W m^{-2} K^{-1}. This method of using the process assessment as a prior and updating it with CERES-era evidence is consistent with how the historical and paleoclimate evidence are used to produce the posterior in SW20. However, there have been substantial updates to the process evidence since SW20 that are currently being synthesized, hence the results here are illustrative based on SW20's published result.

SW20 also showed results using an alternative uniform-S prior, but uniform-S produces pathological results in our case: a uniform prior on S induces a density proportional to $1/\lambda^2$ for $\lambda_{2\text{xCO}_2}$, and because $\mathcal{L}_N$ is high at near-zero values of $\lambda_{2\text{xCO}_2}$, a uniform-S posterior concentrates the probability density at the truncated upper bound on S. Hence instead of uniform S, the lognormal prior here serves as an plausible alternative prior that places high weight on high values of S.

3.3 Posterior Distributions

Posterior probability density functions (PDFs) are proportional to the product of the likelihood and prior PDF. For each prior, Figure 3 includes two versions of the posterior that differ by time period (starting in 2001 versus 2006). 2001–2024 is shown for comparison only. In SI Fig. S4, we also test using 2006–2024 with $+0.15\ \mathrm{W\,m^{-2}\,dec^{-1}}$ added to $\dot{F}$ (described in Section 2.1).

For 2006–2024, the posterior medians (and 66% ranges) under the uniform-λ prior are -0.78 $(-1.68, 0.10)$ $\mathrm{W\,m^{-2}\,K^{-1}}$ for $\lambda_{2\mathrm{xCO_2}}$ and 3.6 $(2.1, 7.6)$ K for S. The lognormal prior yields an S of 4.8 $(2.9, 8.8)$ K, whereas the SW20 process prior yields 3.3 $(2.5, 4.8)$ K. With the additional ERFaci (SI Fig. S4), the S estimates are 2.7 $(1.7, 5.4)$ K using the uniform-λ prior, 4.0 $(2.4, 7.3)$ K using the lognormal prior, and 3.0 $(2.3, 4.3)$ K using the process prior. All posterior ranges are shown in SI Table S2, and posteriors obtained using the $\mathcal{L}_T$ likelihoods are shown for comparison in SI Fig. S5.

The key result for the posteriors is that the ranges for $\lambda_{2\mathrm{xCO_2}}$ and S overlap substantially with estimates from other lines of evidence, e.g., with the existing ranges from SW20 and Forster et al. (2021) and even with the narrower 90% range for S of 2.1–4.0 K in Cooper et al. (2026b). This overlap exists for all three priors, although the lognormal prior results in posterior medians that are at the high end or outside of published 90% ranges for S. The recent trends disfavor $\lambda_{2\mathrm{xCO_2}} < -3\ \mathrm{W\,m^{-2}\,K^{-1}}$ and low S ($<$ 2 K), but the existing historical constraint based on energy-budget changes since 1850 rules out $S < 2$ K even more strongly, as shown in SI Fig. S3 (Cooper et al., 2026a). Overall, the likelihoods based on CERES-era trends in this study are consistent with the historical likelihoods from energy-budget changes over 1850–2023, but the CERES-era trends provide a weaker constraint on both low and high S (SI Fig. S3). The upper bounds of S in Fig. 3d are largely determined by the priors (more so than for the existing historical constraint based on 1850–2023), which is expected given that $\mathcal{L}_N$ evaluated at $\lambda_{2\mathrm{xCO_2}} \approx 0\ \mathrm{W\,m^{-2}\,K^{-1}}$ has a high relative likelihood.

4 Discussion

Estimates of climate sensitivity based on 21st-century trends in Earth's energy imbalance have a wide range but are consistent with other lines of evidence, and they further disfavor low values of S ($<$ 2 K). While the maximum likelihood for S is 5.2 K based on trends over 2006–2024, the posterior medians are 3.6 K with a standard uniform-λ prior, 3.3 K using a process prior from SW20, or 4.8 K under a sensitivity test with a lognormal prior. An important reason why trends starting in 2001 rather than 2006 imply higher S—the plug-in estimates of trends over 2001–2024 suggest 7.7 K, as in Stevens et al. (2026)—is because F does not increase linearly over that period: anthropogenic aerosols and natural forcings cause a decrease in total F over 2001–2006, then F increases linearly over 2006–2024. Thus 2006–2024 is a more reliable period for estimating the feedback from linear trends. Nevertheless, plug-in estimates of the trends over 2006–2024 still suggest high S of 5.2 K and $\lambda_{2\mathrm{xCO_2}}$ of $-0.76\ \mathrm{W\,m^{-2}\,K^{-1}}$, which motivates further investigation into what is causing central estimates of the CERES-era trends to suggest such high S compared to other lines of evidence (Sherwood et al., 2020; Forster et al., 2021; Cooper et al., 2024, 2026a, 2026b; Zelinka et al., 2026). Stevens et al. (2026) raise the following questions: 1) is S truly as high as implied by the trends' central estimates, 2) is the noise from internal variability affecting the trend-based estimates, or 3) are our central estimates of $\dot{F}$, $\dot{N}$, $\dot{T}$, or $\Delta\lambda$ wrong?

It is difficult to rule out noise from internal variability as the explanation based on the internal variability estimated by AGCMs and coupled models. AGCM simulations of $\lambda_{dt} = \dot{R}/\dot{T}$ for 2006–2023 (using time-varying prescribed SST/SIC and constant forcing) suggest that λ_{dt} could have a 90% interval with half-width of $\pm 0.3\ \mathrm{W\,m^{-2}\,K^{-1}}$ from atmospheric noise alone (SI Text S1) (Cooper et al., 2026a). Coupled simulations of 1%-CO_2 ramping also show that λ_{dt} over windows of approximately 20 years varies widely and can differ substantially from $\lambda_{2\mathrm{xCO_2}}$ even under highly idealized CO_2 forcing (i.e., without influences from time-varying aerosol forcing or aerosol-driven pattern effects). For example, CESM2's λ_{dt} varies from -0.6 to -2.0 and back to $-0.6\ \mathrm{W\,m^{-2}\,K^{-1}}$ over years 30–60 of 1%-CO_2, while its $\lambda_{2\mathrm{xCO_2}}$ is $-1.1\ \mathrm{W\,m^{-2}\,K^{-1}}$ (Dvorak et al., 2025); GFDL-ESM4 and MPI-ESM1.2-HR behave similarly (SI Fig. S6) (Danabasoglu et al., 2020; Dunne et al., 2020; Mauritsen et al., 2019).

Errors in the central estimate of forcing could be substantial (Van Loon et al., 2025), especially for ERFaci, although not all recent studies agree on how Forster et al. (2025)'s $\dot{F}$ should be revised (Raghuraman et al., 2023; Hodnebrog et al., 2024; Park & Soden, 2025; Ceppi et al., 2026b; Yuan et al., 2026). We include additional structural uncertainty in $\dot{F}$ and a test with $+0.15\ \mathrm{W\,m^{-2}\,dec^{-1}}$ added to ERFaci trends, based on Yuan et al. (2026)'s results and Van Loon et al. (2025). The additional $+0.15\ \mathrm{W\,m^{-2}\,dec^{-1}}$ ERFaci leads to a maximum likelihood of $S = 3.2$ K and posterior ranges that are more closely aligned with existing estimates. Furthermore, it makes AGCM simulations of $\dot{R}$ align more closely with CERES-based central estimates of $\dot{N}-\dot{F}$ (SI Fig. S7), improving the reported underestimation of R trends in AGCMs (Raghuraman et al., 2021; Hodnebrog et al., 2024).

The CERES-era trends can be used to inform estimates of climate sensitivity in a Bayesian framework (Sherwood et al., 2020; Stevens et al., 2016), so long as the large uncertainties are included in the analysis. The constraint here provides a consistency check with the existing historical line of evidence (c. 1850–present, SI Fig. S3), but both constraints are similar in that they largely eliminate very low S but contain little information about the upper bound (Sherwood et al., 2020; Cooper et al., 2026a). The CERES-era trend could be added as a joint constraint with the existing historical evidence, but more work is needed to investigate the degree to which the trend-based constraint is conditionally independent of the existing historical evidence and the potential correlation of errors. Our posterior results using the process-λ prior from SW20 (Fig. 3) suggest that the CERES-era trends are not likely to cause a substantial change in posterior estimates of S, especially if paleoclimate constraints are also included (Cooper et al., 2024, 2026b). Nevertheless, understanding why the central estimates of trends over the CERES era suggest higher climate sensitivity than other lines of evidence is important, particularly because observation quality over the 21st century is much higher than in other periods. Given potential errors in the decomposition of shortwave/longwave and cloud/clear-sky components of CERES trends (Park & Soden, 2026) and their bearing on emergent constraints that rely on those decompositions, we only use the net radiation trend, which is robust across CERES-based and in situ ocean-based estimates (Loeb et al., 2021; Hakuba et al., 2024).

We suggest one substantial change to the likelihood methods compared to SW20 (Fig. 2). Our proposed change is simple: evaluate N-based likelihoods (of the form $N = F+\lambda T$, with Gaussian error in N) instead of T-based likelihoods ($T = \frac{N-F}{\lambda}$, with Gaussian error in T). This change addresses issues with likelihood methods discussed by Lewis (2023) while maintaining consistency with SW20's Bayesian framework. We expect that revising the likelihood method would tend to give higher weight to high S in the historical and paleoclimate lines of evidence.

In summary, central estimates of the 2006–2024 energy-budget trends favor a weakly stabilizing feedback and a relatively high climate sensitivity: the maximum likelihood is 5.2 K, but the posterior median is 3.6 K using a standard uniform-λ prior or 3.3 K using SW20's process-λ prior. Estimates based on 2001–2024 trends are even higher, but trend-based estimates from this period are less reliable because the forcing does not evolve linearly over 2001–2024. Despite the high values of climate sensitivity produced by central estimates of the trends, the CERES record does not require S outside of existing assessed ranges: after propagating uncertainty in $\dot{N}$, $\dot{F}$, $\dot{T}$, and $\Delta\lambda$, the posterior ranges are consistent with other lines of evidence. The posteriors disfavor low climate sensitivity ($S < 2$ K), but not as strongly as existing constraints based on historical changes over 1850–2023. 21st-century trends provide little information about climate sensitivity's upper bound, which must come from priors or other lines of evidence. We find that the inference of λ_{2xCO_2} and S depends materially on how the likelihood function is constructed, and we advocate for a revised method that evaluates an N-based likelihood rather than the existing T-based likelihood; the N-based method more closely follows the physical energy-balance model and avoids down-weighting high values of S a priori. Continued CERES observations and improved estimates of forcing, pattern effects, and internal variability will be needed to fully explain why the central estimates of CERES-era trends suggest high climate sensitivity, although the posterior ranges are consistent with other lines of evidence.

Open Research Section

Data are available from the following sources: CERES EBAF Ed4.2.1 (Loeb et al., 2018); HadCRUT5.1 (Morice et al., 2021); IGCC forcing (`github.com/ClimateIndicator/forcing-timeseries/releases/tag/v6.3.1`; Smith et al., 2025); and CMIP6 output (`metagrid.esgf-west.org`; Eyring et al., 2016). AGCM results from Cooper et al. (2026a) are available at `https://doi.org/10.31223/X5NF62`. The likelihood calculations are available at `github.com/vtcooper/likelihood_demo.git` and will be archived on Zenodo upon acceptance. Webb (2020) code for calculating S is available at `doi.org/10.5281/zenodo.3945275`.

Conflict of Interest Declaration

The author declares there are no conflicts of interest.

AI Tools Disclosure

Codex was used to review the author's code.

Acknowledgments

V.T.C. acknowledges funding from a Houghton Postdoctoral Fellowship and computing support from Casper (`https://ncar.pub/casper`) and Derecho (`https://doi.org/10.5065/qx9a-pg09`), provided by the NSF National Center for Atmospheric Research (NCAR). Jonathan Gregory, Moritz Günther, and Chongxing Fan ran the AGCM simulations with HadAM3, MPI-ESM1.2-LR, and GFDL-AM4, respectively, in Cooper et al. (2026a). Yi-Ling Hwong, Maria Rugenstein, Jonathan Gregory, Helene Gloeckner, Kyle Armour, Priyam Raghuraman, Cristi Proistosescu, and Bjorn Stevens provided helpful discussions that motivated and informed this study.

References

Allan, R. P., & Merchant, C. J. (2025). Reconciling Earth's growing energy imbalance with ocean warming. *Environmental Research Letters*, *20*(4), 044002. Retrieved from `https://iopscience.iop.org/article/10.1088/1748-9326/adb448` doi: 10.1088/1748-9326/adb448

Andrews, T. (2014). Using an AGCM to Diagnose Historical Effective Radiative Forcing and Mechanisms of Recent Decadal Climate Change. *Journal of Climate*, *27*(3), 1193–1209. Retrieved from `http://journals.ametsoc.org/doi/10.1175/JCLI-D-13-00336.1` doi: 10.1175/JCLI-D-13-00336.1

Andrews, T., Bodas-Salcedo, A., Gregory, J. M., Dong, Y., Armour, K. C., Paynter, D., … Liu, C. (2022). On the Effect of Historical SST Patterns on Radiative Feedback. *Journal of Geophysical Research: Atmospheres*, *127*(18). Retrieved from `https://onlinelibrary.wiley.com/doi/10.1029/2022JD036675` doi: 10.1029/2022JD036675

Andrews, T., Gregory, J. M., Paynter, D., Silvers, L. G., Zhou, C., Mauritsen, T., … Titchner, H. (2018). Accounting for Changing Temperature Patterns Increases Historical Estimates of Climate Sensitivity. *Geophysical Research Letters*, *45*(16), 8490–8499. Retrieved from `https://onlinelibrary.wiley.com/doi/10.1029/2018GL078887` doi: 10.1029/2018GL078887

Andrews, T., Gregory, J. M., & Webb, M. J. (2015). The Dependence of Radiative Forcing and Feedback on Evolving Patterns of Surface Temperature Change in Climate Models. *Journal of Climate*, *28*(4), 1630–1648. Retrieved from https://journals.ametsoc.org/view/journals/clim/28/4/jcli-d-14-00545.1.xml doi: 10.1175/JCLI-D-14-00545.1

Armour, K. C. (2017). Energy budget constraints on climate sensitivity in light of inconstant climate feedbacks. *Nature Climate Change*, *7*(5), 331–335. Retrieved from http://www.nature.com/articles/nclimate3278 doi: 10.1038/nclimate3278

Armour, K. C., Bitz, C. M., & Roe, G. H. (2013). Time-Varying Climate Sensitivity from Regional Feedbacks. *Journal of Climate*, *26*(13), 4518–4534. Retrieved from http://journals.ametsoc.org/doi/10.1175/JCLI-D-12-00544.1 doi: 10.1175/JCLI-D-12-00544.1

Bodman, R. W., & Jones, R. N. (2016). Bayesian estimation of climate sensitivity using observationally constrained simple climate models. *WIREs Climate Change*, *7*(3), 461–473. Retrieved from https://wires.onlinelibrary.wiley.com/doi/10.1002/wcc.397 doi: 10.1002/wcc.397

Ceppi, P., Bodas-Salcedo, A., Zelinka, M. D., Andrews, T., Brient, F., Chadwick, R., … Wing, A. A. (2026a). The Cloud Feedback Model Intercomparison Project (CFMIP) contribution to CMIP7. *EGUsphere*. Retrieved from https://egusphere.copernicus.org/preprints/2026/egusphere-2026-398/ doi: 10.5194/egusphere-2026-398

Ceppi, P., & Gregory, J. M. (2019). A refined model for the Earth's global energy balance. *Climate Dynamics*, *53*(7-8), 4781–4797. Retrieved from http://link.springer.com/10.1007/s00382-019-04825-x doi: 10.1007/s00382-019-04825-x

Ceppi, P., Wilson Kemsley, S., Andersen, H., Andrews, T., Kramer, R. J., Nowack, P., … Zelinka, M. D. (2026b). Emerging low-cloud feedback and adjustment in global satellite observations. *Atmospheric Chemistry and Physics*, *26*(6), 4153–4171. Retrieved from https://acp.copernicus.org/articles/26/4153/2026/ doi: 10.5194/ACP-26-4153-2026

Chan, D., Chan, S. C., Siddons, J. T., Cable, A., Faulkner, A., Cornes, R. C., … Huybers, P. (2026). DCENT-I: A Globally Infilled Extension of the Dynamically Consistent ENsemble of Temperature Dataset. *Geoscience Data Journal*, *13*(2), 70054. Retrieved from https://rmets.onlinelibrary.wiley.com/doi/10.1002/gdj3.70054 doi: 10.1002/gdj3.70054

Charney, J. G., Arakawa, A., Baker, D. J., Bolin, B., Dickinson, R. E., Goody, R. M., … Wunsch, C. I. (1979). *Carbon dioxide and climate: a scientific assessment*. National Academy of Sciences, Washington, DC.

Chen, Y.-T., Merlis, T. M., Dinh, T., Griffies, S. M., Krasting, J., Dussin, R., … Fueglistaler, S. A. (2026). Assessing Earth's Energy Imbalance Trend in the Early 21st Century in Two High-Resolution Coupled Models. Retrieved from https://agupubs.onlinelibrary.wiley.com/doi/10.1029/2025GL121277 doi: 10.1029/2025GL121277

Cooper, V. T., Armour, K. C., Gregory, J. M., Andrews, T., Guenther, M., & Fan, C. (2026a). Historical Pattern Effects and Climate Sensitivity Revisited with Novel Constraints on Past Warming Patterns. *EarthArXiv*. Retrieved from https://doi.org/10.31223/X5NF62 doi: 10.31223/X5NF62

Cooper, V. T., Armour, K. C., Hakim, G. J., Tierney, J. E., Burls, N. J., Proistosescu, C., … Dong, Y. (2026b). Paleoclimate pattern effects help constrain climate sensitivity and 21st-century warming. *Proceedings of the National Academy of Sciences*, *123*(4). Retrieved from https://pnas.org/doi/10.1073/pnas.2511370123 doi: 10.1073/pnas.2511370123

Cooper, V. T., Armour, K. C., Hakim, G. J., Tierney, J. E., Osman, M. B., Proistosescu, C., … Chmielowiec, P. (2024). Last Glacial Maximum pattern effects reduce climate sensitivity estimates. *Science Advances*, *10*(16), 9461. Retrieved from https://www.science.org/doi/10.1126/sciadv.adk9461 doi: 10.1126/sciadv.adk9461

Cooper, V. T., Hakim, G. J., & Armour, K. C. (2025). Monthly Sea Surface Temperature, Sea Ice, and Sea Level Pressure over 1850–2023 from Coupled Data Assimilation. *Journal of Climate*, *38*(19), 5461–5490. Retrieved from https://doi.org/10.1175/JCLI-D-25-0021.1 doi: 10.1175/JCLI-D-25-0021.1

Danabasoglu, G., Lamarque, J., Bacmeister, J., Bailey, D. A., DuVivier, A. K., Edwards, J., … Strand, W. G. (2020). The Community Earth System Model Version 2 (CESM2). *Journal of Advances in Modeling Earth Systems*, *12*(2). Retrieved from https://onlinelibrary.wiley.com/doi/10.1029/2019MS001916 doi: 10.1029/2019MS001916

Dunne, J. P., Horowitz, L. W., Adcroft, A. J., Ginoux, P., Held, I. M., John, J. G., … Zhao, M. (2020). The GFDL Earth System Model Version 4.1 (GFDL-ESM 4.1): Overall Coupled Model Description and Simulation Characteristics. *Journal of Advances in Modeling Earth Systems*, *12*(11). Retrieved from `https://agupubs.onlinelibrary.wiley.com/doi/10.1029/2019MS002015` doi: 10.1029/2019MS002015

Dvorak, M., Armour, K. C., Feng, R., Cooper, V. T., Zhu, J., Burls, N., & Proistosescu, C. (2025). Mid-Pliocene Climate Forcing, Sea Surface Temperature Patterns, and Implications for Modern-Day Climate Sensitivity. *Journal of Climate*, *38*(13), 3037–3053. Retrieved from `https://journals.ametsoc.org/view/journals/clim/38/13/JCLI-D-24-0410.1.xml` doi: 10.1175/JCLI-D-24-0410.1

Eyring, V., Bony, S., Meehl, G. A., Senior, C. A., Stevens, B., Stouffer, R. J., & Taylor, K. E. (2016). Overview of the Coupled Model Intercomparison Project Phase 6 (CMIP6) experimental design and organization. *Geoscientific Model Development*, *9*(5), 1937–1958. Retrieved from `https://gmd.copernicus.org/articles/9/1937/2016/` doi: 10.5194/gmd-9-1937-2016

Fan, C., Paynter, D., Kramer, R. J., & Lin, P. (2025). Sensitivity of Earth's Radiation Budget to Lower Boundary Condition Data Sets in Historical Climate Simulations. *Geophysical Research Letters*, *52*(17). Retrieved from `https://agupubs.onlinelibrary.wiley.com/doi/10.1029/2025GL115914` doi: 10.1029/2025GL115914

Forster, P., Storelvmo, T., Armour, K., Collins, W., Dufresne, J.-L., Frame, D., … Zhang, H. (2021). The Earth's energy budget, climate feedbacks, and climate sensitivity. In V. Masson-Delmotte et al. (Eds.), *Climate change 2021: The physical science basis. contribution of working group i to the sixth assessment report of the intergovernmental panel on climate change* (chap. 7). Cambridge, UK and New York, NY: Cambridge University Press. doi: 10.1017/9781009157896.009

Forster, P. M., Smith, C., Walsh, T., Lamb, W. F., Lamboll, R., Cassou, C., … Zhai, P. (2025). Indicators of Global Climate Change 2024: annual update of key indicators of the state of the climate system and human influence. *Earth System Science Data*, *17*(6), 2641–2680. Retrieved from https://essd.copernicus.org/articles/17/2641/2025/ doi: 10.5194/essd-17-2641-2025

Frame, D. J., Booth, B. B. B., Kettleborough, J. A., Stainforth, D. A., Gregory, J. M., Collins, M., & Allen, M. R. (2005). Constraining climate forecasts: The role of prior assumptions. *Geophysical Research Letters*, *32*(9). Retrieved from https://agupubs.onlinelibrary.wiley.com/doi/10.1029/2004GL022241 doi: 10.1029/2004GL022241

Gelman, A., Carlin, J. B., Stern, H. S., Dunson, D. B., Vehtari, A., & Rubin, D. B. (2013). *Bayesian Data Analysis*. Chapman and Hall/CRC. Retrieved from https://www.taylorfrancis.com/books/9781439898208 doi: 10.1201/b16018

Gelman, A., Jakulin, A., Pittau, M. G., & Su, Y.-S. (2008). A weakly informative default prior distribution for logistic and other regression models. *The Annals of Applied Statistics*, *2*(4), 1360–1383. Retrieved from https://doi.org/10.1214/08-AOAS191 doi: 10.1214/08-AOAS191

Gelman, A., Simpson, D., & Betancourt, M. (2017). The Prior Can Often Only Be Understood in the Context of the Likelihood. *Entropy*, *19*(10), 555. Retrieved from https://doi.org/10.3390/e19100555 doi: 10.3390/e19100555

Gelman, A., Vehtari, A., Simpson, D., Margossian, C. C., Carpenter, B., Yao, Y., … Modrák, M. (2020). Bayesian Workflow. *arXiv*. Retrieved from http://arxiv.org/abs/2011.01808

Goessling, H. F., Rackow, T., & Jung, T. (2025). Recent global temperature surge intensified by record-low planetary albedo. *Science*, *387*(6729), 68–73. Retrieved from https://www.science.org/doi/10.1126/science.adq7280 doi: 10.1126/science.adq7280

Goodwin, P. (2021). Probabilistic projections of future warming and climate sensitivity trajectories. *Oxford Open Climate Change*, *1*(1). Retrieved from https://academic.oup.com/oocc/article/doi/10.1093/oxfclm/kgab007/6326790 doi: 10.1093/oxfclm/kgab007

Goodwin, P., & Cael, B. B. (2021). Bayesian estimation of Earth's climate sensitivity and transient climate response from observational warming and heat content datasets. *Earth System Dynamics*, *12*(2), 709–723. Retrieved from https://esd.copernicus.org/articles/12/709/2021/ doi:

10.5194/esd-12-709-2021

Gregory, J. M., & Andrews, T. (2016). Variation in climate sensitivity and feedback parameters during the historical period. *Geophysical Research Letters*, *43*(8), 3911–3920. Retrieved from https://agupubs.onlinelibrary.wiley.com/doi/10.1002/2016GL068406 doi: 10.1002/2016GL068406

Gregory, J. M., Stouffer, R. J., Raper, S. C. B., Stott, P. A., & Rayner, N. A. (2002). An Observationally Based Estimate of the Climate Sensitivity. *Journal of Climate*, *15*(22), 3117–3121. Retrieved from http://journals.ametsoc.org/doi/10.1175/1520-0442(2002)015<3117:AOBEOT>2.0.CO;2 doi: 10.1175/1520-0442(2002)015<3117:AOBEOT>2.0.CO;2

Hakuba, M. Z., Fourest, S., Boyer, T., Meyssignac, B., Carton, J. A., Forget, G., … von Schuckmann, K. (2024). Trends and Variability in Earth's Energy Imbalance and Ocean Heat Uptake Since 2005. *Surveys in Geophysics*, *45*(6), 1721–1756. Retrieved from https://link.springer.com/10.1007/s10712-024-09849-5 doi: 10.1007/s10712-024-09849-5

Hansen, J. E., Kharecha, P., Sato, M., Tselioudis, G., Kelly, J., Bauer, S. E., … Pokela, A. (2025). Global Warming Has Accelerated: Are the United Nations and the Public Well-Informed? *Environment: Science and Policy for Sustainable Development*, *67*(1), 6–44. Retrieved from https://www.tandfonline.com/doi/full/10.1080/00139157.2025.2434494 doi: 10.1080/00139157.2025.2434494

Hodnebrog, Ø., Myhre, G., Jouan, C., Andrews, T., Forster, P. M., Jia, H., … Schulz, M. (2024). Recent reductions in aerosol emissions have increased Earth's energy imbalance. *Communications Earth & Environment*, *5*(1), 166. Retrieved from https://www.nature.com/articles/s43247-024-01324-8 doi: 10.1038/s43247-024-01324-8

Johnson, G. C., Lyman, J. M., & Loeb, N. G. (2016). Improving estimates of Earth's energy imbalance. *Nature Climate Change*, *6*(7), 639–640. Retrieved from https://www.nature.com/articles/nclimate3043 doi: 10.1038/nclimate3043

Lewis, N. (2014). Objective Inference for Climate Parameters: Bayesian, Transformation-of-Variables, and Profile Likelihood Approaches. *Journal of Climate*, *27*(19), 7270–7284. Retrieved from http://journals.ametsoc.org/

doi/10.1175/JCLI-D-13-00584.1 doi: 10.1175/JCLI-D-13-00584.1

Lewis, N. (2023). Objectively combining climate sensitivity evidence. *Climate Dynamics*, *60*(9-10), 3139–3165. Retrieved from https://link.springer.com/10.1007/s00382-022-06468-x doi: 10.1007/s00382-022-06468-x

Loeb, N. G., Doelling, D. R., Wang, H., Su, W., Nguyen, C., Corbett, J. G., … Kato, S. (2018). Clouds and the Earth's Radiant Energy System (CERES) Energy Balanced and Filled (EBAF) Top-of-Atmosphere (TOA) Edition-4.0 Data Product. *Journal of Climate*, *31*(2), 895–918. Retrieved from https://journals.ametsoc.org/doi/10.1175/JCLI-D-17-0208.1 doi: 10.1175/JCLI-D-17-0208.1

Loeb, N. G., Johnson, G. C., Thorsen, T. J., Lyman, J. M., Rose, F. G., & Kato, S. (2021). Satellite and Ocean Data Reveal Marked Increase in Earth's Heating Rate. *Geophysical Research Letters*, *48*(13). Retrieved from https://agupubs.onlinelibrary.wiley.com/doi/10.1029/2021GL093047 doi: 10.1029/2021GL093047

Loeb, N. G., Mayer, M., Kato, S., Fasullo, J. T., Zuo, H., Senan, R., … Balmaseda, M. (2022). Evaluating Twenty-Year Trends in Earth's Energy Flows From Observations and Reanalyses. *Journal of Geophysical Research: Atmospheres*, *127*(12). Retrieved from https://agupubs.onlinelibrary.wiley.com/doi/10.1029/2022JD036686 doi: 10.1029/2022JD036686

Marvel, K., & Webb, M. (2025). Towards robust community assessments of the Earth's climate sensitivity. *Earth System Dynamics*, *16*(1), 317–332. Retrieved from https://esd.copernicus.org/articles/16/317/2025/ doi: 10.5194/esd-16-317-2025

Mauritsen, T., Bader, J., Becker, T., Behrens, J., Bittner, M., Brokopf, R., … Roeckner, E. (2019). Developments in the MPI-M Earth System Model version 1.2 (MPI-ESM1.2) and Its Response to Increasing CO2. *Journal of Advances in Modeling Earth Systems*, *11*(4), 998–1038. Retrieved from https://agupubs.onlinelibrary.wiley.com/doi/10.1029/2018MS001400 doi: 10.1029/2018MS001400

Mauritsen, T., Tsushima, Y., Meyssignac, B., Loeb, N. G., Hakuba, M., Pilewskie, P., … Zelinka, M. D. (2025). Earth's Energy Imbalance More Than Doubled in Recent Decades. *AGU Advances*, *6*(3). Retrieved from https://

agupubs.onlinelibrary.wiley.com/doi/10.1029/2024AV001636 doi: 10.1029/2024AV001636

Morice, C. P., Kennedy, J. J., Rayner, N. A., Winn, J. P., Hogan, E., Killick, R. E., … Simpson, I. R. (2021). An Updated Assessment of Near-Surface Temperature Change From 1850: The HadCRUT5 Data Set. *Journal of Geophysical Research: Atmospheres*, *126*(3). Retrieved from https://agupubs.onlinelibrary.wiley.com/doi/10.1029/2019JD032361 doi: 10.1029/2019JD032361

Park, C., & Soden, B. (2026). Reconciling Discrepancies Between Observed and Model-Simulated Cloud Radiative Trends and Their Implications for Earth's Energy Imbalance. *Research Square*. Retrieved from https://www.researchsquare.com/article/rs-9054442/v2 doi: 10.21203/rs.3.rs-9054442/v2

Park, C., & Soden, B. J. (2025). Negligible contribution from aerosols to recent trends in Earth's energy imbalance. *Science Advances*, *11*(48), eadv9429. Retrieved from https://www.science.org/doi/10.1126/sciadv.adv9429 doi: 10.1126/sciadv.adv9429

Pueyo, S. (2012). Solution to the paradox of climate sensitivity. *Climatic Change*, *113*(2), 163–179. Retrieved from http://link.springer.com/10.1007/s10584-011-0328-x doi: 10.1007/s10584-011-0328-x

Raghuraman, S. P., Paynter, D., Menzel, R., & Ramaswamy, V. (2023). Forcing, Cloud Feedbacks, Cloud Masking, and Internal Variability in the Cloud Radiative Effect Satellite Record. *Journal of Climate*, *36*(12), 4151–4167. Retrieved from https://journals.ametsoc.org/view/journals/clim/36/12/JCLI-D-22-0555.1.xml doi: 10.1175/JCLI-D-22-0555.1

Raghuraman, S. P., Paynter, D., & Ramaswamy, V. (2021). Anthropogenic forcing and response yield observed positive trend in Earth's energy imbalance. *Nature Communications*, *12*(1), 4577. Retrieved from https://www.nature.com/articles/s41467-021-24544-4 doi: 10.1038/s41467-021-24544-4

Rugenstein, M., Zelinka, M., Karnauskas, K., Ceppi, P., & Andrews, T. (2023). Patterns of Surface Warming Matter for Climate Sensitivity. *Eos*, *104*. Retrieved from https://doi.org/10.1029/2023EO230411 doi: 10.1029/2023EO230411

Rugenstein, M. A., & Armour, K. C. (2021). Three Flavors of Radiative Feedbacks and Their Implications for Estimating Equilibrium Climate Sensitivity. *Geophysical Research Letters*, *48*(15). doi: 10.1029/2021GL092983

Schmidt, G. A., Andrews, T., Bauer, S. E., Durack, P. J., Loeb, N. G., Ramaswamy, V., … Ziehn, T. (2023). CERESMIP: a climate modeling protocol to investigate recent trends in the Earth's Energy Imbalance. *Frontiers in Climate*, *5*. Retrieved from `https://www.frontiersin.org/articles/10.3389/fclim.2023.1202161/full` doi: 10.3389/fclim.2023.1202161

Sherwood, S. C., Webb, M. J., Annan, J. D., Armour, K. C., Forster, P. M., Hargreaves, J. C., … Zelinka, M. D. (2020). An Assessment of Earth's Climate Sensitivity Using Multiple Lines of Evidence. *Reviews of Geophysics*, *58*(4). Retrieved from `https://onlinelibrary.wiley.com/doi/10.1029/2019RG000678` doi: 10.1029/2019RG000678

Smith, C., Walsh, T., Gillett, N., Hauser, M., Krummel, P., Lamb, W., … Forster, P. (2025). Indicators of Global Climate Change 2024. *Zenodo.* Retrieved from `https://doi.org/10.5281/zenodo.15744430` doi: 10.5281/zenodo.15744430

Stevens, B., Andrews, T., Bender, F. A.-M., Bony, S., Ceppi, P., Glassmeier, F., … Wilcox, L. J. (2026). Earth's net incoming energy-flux imbalance (and its implications for understanding climate change). *Reports on Earth System Science (2026 Ringberg Workshop, MPI-M).* Retrieved from `https://doi.org/10.17617/2.3711842` doi: 10.17617/2.3711842

Stevens, B., Sherwood, S. C., Bony, S., & Webb, M. J. (2016). Prospects for narrowing bounds on Earth's equilibrium climate sensitivity. *Earth's Future*, *4*(11), 512–522. Retrieved from `https://agupubs.onlinelibrary.wiley.com/doi/10.1002/2016EF000376` doi: 10.1002/2016EF000376

Tam, R. Y. S., Myers, T. A., Zelinka, M. D., Proistosescu, C., Lin, Y.-J., & Marvel, K. (2026). Meteorological drivers of the low-cloud radiative feedback pattern effect and its uncertainty. *Atmospheric Chemistry and Physics*, *26*(6), 4289–4311. Retrieved from `https://acp.copernicus.org/articles/26/4289/2026/` doi: 10.5194/acp-26-4289-2026

Thorne, P. W., Nicklas, J. M., Kennedy, J. J., Calvert, B., Fox-Kemper, B., Richardson, M. T., … Murtagh, E. (2026). *How well can we quan-*

tify when 1.5 °C of global warming has been exceeded? Retrieved from https://essd.copernicus.org/preprints/essd-2025-825/ doi: 10.5194/essd-2025-825

Van Loon, S., Rugenstein, M., & Barnes, E. A. (2025). Observation-based estimate of Earth's effective radiative forcing. *Proceedings of the National Academy of Sciences*, *122*(24), e2425445122. Retrieved from https://pnas.org/doi/10.1073/pnas.2425445122 doi: 10.1073/pnas.2425445122

Webb, M. (2020). *Code and Data for WCRP Climate Sensitivity Assessment* (Tech. Rep.). doi: 10.5281/zenodo.3945275

Yuan, T., Song, H., Kramer, R., Oreopoulos, L., Raghuraman, S. P., Wood, R., & Chin, M. (2026). Aerosol effective radiative forcing increases Earth's energy imbalance in recent decades. *Nature Communications*, *17*(1), 6322. Retrieved from https://www.nature.com/articles/s41467-026-72926-3 doi: 10.1038/s41467-026-72926-3

Zelinka, M. D., Myers, T. A., Qin, Y., Chao, L.-W., Klein, S. A., Po-Chedley, S., … Gettelman, A. (2026). Recent cloud trends and extremes reaffirm established bounds on cloud feedback and aerosol-cloud interactions. *Communications Earth & Environment*. Retrieved from https://www.nature.com/articles/s43247-026-03461-8 doi: 10.1038/s43247-026-03461-8

Supporting Information for “Climate Sensitivity from 21st-Century Trends in Earth’s Energy Imbalance”

Vincent T. Cooper[1]

[1]Department of Earth, Atmospheric, and Planetary Sciences, Massachusetts Institute of Technology, Cambridge, MA, USA

Contents of this file

Text S1: Estimating Uncertainty in $\Delta\lambda$

We estimate uncertainty in $\Delta\lambda$ estimates from the spread across AGCMs, SST and sea ice concentration (SIC), and atmospheric noise. Because the set of simulations in Cooper et al. (2026) is incomplete (we do not have every SST/SIC pattern in every AGCM), we analyze two subsets separately: four AGCMs containing all 14 SST/SIC patterns and all six AGCMs containing the same three patterns.

For each subset, we use a two-way random-effects decomposition to estimate the variance across equally weighted AGCMs and SST/SIC patterns. We combine the model, pattern, and model–pattern interaction terms into a single structural component representing uncertainty associated with the choice of AGCM and SST/SIC boundary conditions, including model-dependent responses to the imposed patterns.

Most model–pattern combinations contain only one atmospheric realization, so the contribution of atmospheric noise from initial conditions cannot be estimated directly for each AGCM. We therefore approximate atmospheric internal variability from the 14-member HadAM3 initial-condition ensemble, in which every member uses the same SST/SIC pattern. This gives $\sigma_{\text{atmos}} = 0.128\ \mathrm{W\,m^{-2}\,K^{-1}}$, but we note that HadAM3 appears to have smaller atmospheric variability compared to CAM6 (Cooper et al., 2026). We subtract the atmospheric variance from the total variance across AGCM–pattern combinations and define the remainder as structural variance: $\sigma^2_{\text{struct}} = \sigma^2_{\text{model,pattern}} - \sigma^2_{\text{atmos}}$. This procedure assigns model-pattern interactions and any other systematic differences among model-pattern combinations to structural uncertainty. Although the balanced four-AGCM, 14-pattern subset permits an approximate two-way separation of AGCM main effects from SST/SIC pattern main effects (yielding the percentage attributions reported in the main text), the full ensemble design is incomplete, so all structural terms are pooled here rather than separately identified.

The structural standard deviation is 0.278 $\mathrm{W\,m^{-2}\,K^{-1}}$ in the four-AGCM, 14-pattern subset and 0.272 $\mathrm{W\,m^{-2}\,K^{-1}}$ in the six-AGCM, three-pattern subset. We average the two estimates, obtaining $\sigma_{\text{struct}} = 0.275$ $\mathrm{W\,m^{-2}\,K^{-1}}$. The two subsets overlap and therefore are not independent estimates; their close agreement instead provides a test of sensitivity to the incomplete simulation design. Finally, we add the structural and atmospheric variances: $\sigma_{\Delta\lambda} = \sqrt{\sigma^2_{\text{struct}} + \sigma^2_{\text{atmos}}} = 0.303$ $\mathrm{W\,m^{-2}\,K^{-1}}$.

Excluding atmospheric internal variability gives $\sigma_{\Delta\lambda} \approx 0.27$ $\mathrm{W\,m^{-2}\,K^{-1}}$, showing that the uncertainty estimate is primarily controlled by structural differences among the AGCM–SST/SIC combinations. We use 0.3 $\mathrm{W\,m^{-2}\,K^{-1}}$ as the 1σ uncertainty in $\Delta\lambda$.

If we instead assume that atmospheric variability contributes the same fraction of the total across-pattern variance in every AGCM as in HadAM3, this fraction is $f_{\text{atmos}} = (0.128/0.213)^2 = 0.362$. We estimate each model's atmospheric standard deviation as $\sigma_{\text{atmos},m} = \sigma_{\text{total},m}\sqrt{f_{\text{atmos}}}$, giving 0.125, 0.174, 0.207, and 0.128 $\mathrm{W\,m^{-2}\,K^{-1}}$ for CAM4, CAM5, CAM6, and HadAM3, respectively. Pooling these four variance estimates gives $\sigma_{\text{atmos}} = 0.162$ $\mathrm{W\,m^{-2}\,K^{-1}}$, corresponding to an approximately Gaussian 90% half-width of ± 0.27 $\mathrm{W\,m^{-2}\,K^{-1}}$; using CAM6 alone gives ± 0.34 $\mathrm{W\,m^{-2}\,K^{-1}}$.

Text S2: Why the N- and T-Scored Likelihoods Differ

Here we illustrate why algebraically equivalent forms of the energy budget produce different likelihood functions using two complementary perspectives. First, we focus on the *effective error scales* of the two different forms of the energy-budget equation, then we consider *implicit priors* on $\dot{N}$ and $\dot{T}$.

For simplicity, consider a fixed proposed value of the trend-based feedback,

$$\lambda_{dt} = \lambda_{2\mathrm{xCO}_2} - \Delta\lambda. \tag{1}$$

The trend energy budget is

$$\dot{N} = \dot{F} + \lambda_{dt}\dot{T} + \eta. \tag{2}$$

In $\mathcal{L}_N$, the predicted energy-imbalance trend is

$$\dot{N}_{\mathrm{pred}} = \dot{F} + \lambda_{dt}\dot{T}_{\mathrm{obs}}, \tag{3}$$

and the difference between observed and predicted $\dot{N}$ is

$$r_N = \dot{N}_{\mathrm{obs}} - \dot{N}_{\mathrm{pred}} = \dot{N}_{\mathrm{obs}} - \dot{F} - \lambda_{dt}\dot{T}_{\mathrm{obs}}. \tag{4}$$

Temporarily ignoring covariance between $\dot{N}$ and $\dot{T}$, and assuming that forcing uncertainty is independent of both, the variance of this residual is

$$\sigma_{r_N}^2 = \sigma_N^2 + \sigma_F^2 + \lambda_{dt}^2\sigma_T^2. \tag{5}$$

In this formulation, the energy-budget terms and their errors remain additive in N units.

Rearranging the same budget into T space gives

$$\dot{T}_{\mathrm{pred}} = \frac{\dot{N}_{\mathrm{obs}} - \dot{F}}{\lambda_{dt}}. \tag{6}$$

The difference between observed and predicted $\dot{T}$ is

$$r_T = \dot{T}_{\mathrm{obs}} - \dot{T}_{\mathrm{pred}} = \dot{T}_{\mathrm{obs}} - \frac{\dot{N}_{\mathrm{obs}} - \dot{F}}{\lambda_{dt}} = -\frac{r_N}{\lambda_{dt}}. \tag{7}$$

Its variance is

$$\sigma_{r_T}^2 = \sigma_T^2 + \frac{\sigma_N^2 + \sigma_F^2}{\lambda_{dt}^2} = \frac{\sigma_{r_N}^2}{\lambda_{dt}^2}. \tag{8}$$

When the budget is evaluated in T space, uncertainties in $\dot{N}$ and $\dot{F}$ are divided by $|\lambda_{dt}|$. Therefore, as the magnitude of the feedback approaches zero, even a small uncertainty in $\dot{N} - \dot{F}$ produces a large uncertainty in the predicted $\dot{T}$.

At the plug-in central estimate, both formulations reproduce the central observed trends exactly. However, after uncertainty in $\dot{N}$ and $\dot{F}$ is marginalized, the total uncertainty associated with $\dot{T}_{\text{pred}}$ depends on λ_{dt} and becomes very large as λ_{dt} approaches zero. A Gaussian distribution with a larger uncertainty has a lower peak. Consequently, an exact fit with a very broad uncertainty can have a lower likelihood than a slightly poorer fit with a narrower uncertainty, which is why the maximum likelihoods differ between $\mathcal{L}_T$ and $\mathcal{L}_N$. In this simplified case,

$$\mathcal{L}_T(\lambda_{dt}) = |\lambda_{dt}|\,\mathcal{L}_N(\lambda_{dt}). \tag{9}$$

The factor of $|\lambda_{dt}|$ suppresses $\mathcal{L}_T$ as λ_{dt} approaches zero and gives greater relative weight to feedbacks with larger absolute values.

Now we consider an explanation focused on implicit priors for the true $\dot{N}$ and $\dot{T}$, which also illustrates why the likelihoods differ. An observational error model directly specifies the probability of an observed trend given its true value, for example $p(\dot{T}_{\text{obs}} \mid \dot{T}_{\text{true}})$. Interpreting this uncertainty as a distribution of plausible true trends requires another application of Bayes's theorem: $p(\dot{T}_{\text{true}} \mid \dot{T}_{\text{obs}}) \propto p(\dot{T}_{\text{obs}} \mid \dot{T}_{\text{true}})\, p(\dot{T}_{\text{true}})$.

Treating the observational uncertainty as centered on $\dot{T}_{\text{obs}}$ implicitly assumes that the prior $p(\dot{T}_{\text{true}})$ is uniform over the range relevant to the likelihood calculation. To illustrate the consequence, hold $\dot{F}$ and λ_{dt} fixed and temporarily ignore covariance. The N-scored likelihood integrates over the unknown, latent true temperature trend:

$$\mathcal{L}_N(\lambda_{dt}) \propto \int p\Big(\dot{N}_{\mathrm{obs}} \mid \dot{F} + \lambda_{dt}\dot{T}_{\mathrm{true}}\Big)\, p\Big(\dot{T}_{\mathrm{obs}} \mid \dot{T}_{\mathrm{true}}\Big)\, p(\dot{T}_{\mathrm{true}})\, \mathrm{d}\dot{T}_{\mathrm{true}}. \tag{10}$$

Thus $\mathcal{L}_N$ uses the unknown true $\dot{T}$ as the reference variable and implicitly adopts a locally uniform prior on it.

The T-scored likelihood instead assumes $p(\dot{N}_{\mathrm{true}} \mid \dot{N}_{\mathrm{obs}}) \propto p(\dot{N}_{\mathrm{obs}} \mid \dot{N}_{\mathrm{true}})\, p(\dot{N}_{\mathrm{true}})$, implicitly adopting a locally uniform prior on the unknown true $\dot{N}$, and integrates over the unknown true energy-imbalance trend:

$$\mathcal{L}_T(\lambda_{dt}) \propto \int p\Big(\dot{N}_{\mathrm{obs}} \mid \dot{N}_{\mathrm{true}}\Big)\, p\left(\dot{T}_{\mathrm{obs}} \mid \frac{\dot{N}_{\mathrm{true}} - \dot{F}}{\lambda_{dt}}\right) p(\dot{N}_{\mathrm{true}})\, \mathrm{d}\dot{N}_{\mathrm{true}}. \tag{11}$$

The two uniform priors on $\dot{T}_{\mathrm{true}}$ versus $\dot{N}_{\mathrm{true}}$ are not equivalent under the energy-budget relationship. Substituting

$$\dot{N}_{\mathrm{true}} = \dot{F} + \lambda_{dt}\dot{T}_{\mathrm{true}}, \qquad \mathrm{d}\dot{N}_{\mathrm{true}} = |\lambda_{dt}|\, \mathrm{d}\dot{T}_{\mathrm{true}}, \tag{12}$$

introduces the same factor found from the effective-error-scale derivation above, i.e., $\mathcal{L}_T(\lambda_{dt}) \propto |\lambda_{dt}|\, \mathcal{L}_N(\lambda_{dt})$.

Thus a locally uniform prior on $\dot{T}_{\mathrm{true}}$ implies $p(\dot{N}_{\mathrm{true}} \mid \lambda_{dt}) \propto 1/|\lambda_{dt}|$, whereas a locally uniform prior on $\dot{N}_{\mathrm{true}}$ implies $p(\dot{T}_{\mathrm{true}} \mid \lambda_{dt}) \propto |\lambda_{dt}|$. The two likelihoods therefore represent different assumptions about which true trend is the underlying reference variable. This distinction does not by itself establish that either likelihood is preferable; rather, it shows that neither construction is prior-free.

Our preference for $\mathcal{L}_N$ rests on the physical form of the standard energy-balance model, Eqs. (1) and (4) of the main text, in which unresolved variability enters as an additive energy-budget residual,

$$\eta = \dot{N} - \dot{F} - \lambda_{dt}\dot{T}. \tag{13}$$

We specify the distribution of this residual in N space. Conditional on $\dot{F}$, $\dot{T}$, and λ_{dt}, this form implies a generative model for $\dot{N}$ and therefore the likelihood $\mathcal{L}_N$, while still propagating uncertainty in $\dot{T}$. In contrast, $\mathcal{L}_T$ specifies the Gaussian error model after rearranging the budget into T space. Thus it treats the radiative residual as an additive temperature error, $\eta_T = -\eta \,/\, \lambda_{dt}$, whose scale depends on the proposed feedback and becomes arbitrarily large as $|\lambda_{dt}|$ approaches zero. The implicit-prior and effective-error-scale explanations are two interpretations of the same feedback-dependent weighting.

Our full likelihood calculations account for covariance between $\dot{N}$ and $\dot{T}$ and marginalize over uncertainty in $\dot{F}$ and $\Delta\lambda$, although we find that the covariance has a small impact on the likelihoods. Including the covariance changes the variance of the N-space residual to

$$\sigma_{r_N}^2 = \sigma_N^2 + \sigma_F^2 + \lambda_{dt}^2 \sigma_T^2 - 2\lambda_{dt} c_{NT}. \tag{14}$$

The corresponding relationship $\sigma_{r_T}^2 = \sigma_{r_N}^2 / \lambda_{dt}^2$ remains unchanged. When $\Delta\lambda$ is marginalized, λ_{dt} varies for each value of $\Delta\lambda$, so the factor $|\lambda_{dt}|$ is applied to each likelihood contribution before they are averaged. This same weighting explains the different shapes and maxima of the fully marginalized likelihoods.

Text S3: Likelihood Estimation

This section provides computational details for the $\mathcal{L}_N$ and $\mathcal{L}_T$ marginal likelihoods defined in the main text. For compactness, let $N_o \equiv \dot{N}_{\text{obs}}$ and $T_o \equiv \dot{T}_{\text{obs}}$, and let N and T denote the unknown true values of these trends, not climate-state levels. We define their observational errors as

$$e_N = N_o - N, \qquad e_T = T_o - T. \tag{15}$$

These observational errors are distinct from the residuals r_N and r_T in Text S2, which are the differences between observed and model-predicted trends. We use σ_N^2 and σ_T^2 as shorthand for $\sigma_{\dot{N}}^2$ and $\sigma_{\dot{T}}^2$, respectively, and define

$$\lambda_{dt} = \lambda_{2\text{xCO}_2} - \Delta\lambda. \tag{16}$$

We represent the total errors in the two observed trends as

$$\begin{pmatrix} e_T \\ e_N \end{pmatrix} \sim \mathcal{N}\left[\begin{pmatrix} 0 \\ 0 \end{pmatrix}, \begin{pmatrix} \sigma_T^2 & c_{NT} \\ c_{NT} & \sigma_N^2 \end{pmatrix}\right]. \tag{17}$$

The total variances and covariance used in the likelihood calculation are

$$\begin{aligned} \sigma_N^2 &= \sigma_{N,\text{OLS}}^2, \\ \sigma_T^2 &= \sigma_{T,\text{ens}}^2 + \sigma_{T,\text{IV}}^2, \\ c_{NT} &= c_{NT,\text{IV}}. \end{aligned} \tag{18}$$

The CERES OLS standard error represents the total marginal uncertainty in $\dot{N}$, and we do not add an additional variance to represent internal variability. In contrast, the HadCRUT5.1 ensemble samples observational uncertainty but not alternative realizations of internal variability, so we add $\sigma_{T,\text{IV}}^2$ to its ensemble variance. We estimate c_{NT} from paired $\dot{N}$ and $\dot{T}$ trends in the CESM2 and MPI-ESM1.2-LR preindustrial-control simulations. Including this off-diagonal covariance does not add uncertainty to $\dot{N}$; all marginal uncertainty in $\dot{N}$ remains represented by $\sigma_{N,\text{OLS}}^2$.

We approximate the forcing-trend and pattern-effect uncertainties as

$$
\begin{aligned}
\dot{F} &\sim \mathcal{N}\left(\mu_F, \sigma^2_{F,\mathrm{ens}} + \sigma^2_{F,\mathrm{struct}}\right), \\
\Delta\lambda &\sim \mathcal{N}\left(0, \sigma^2_{\Delta\lambda}\right),
\end{aligned} \tag{19}
$$

where $\sigma_{F,\mathrm{struct}} = 0.1\ \mathrm{W\,m^{-2}\,decade^{-1}}$ and $\sigma_{\Delta\lambda} = 0.3\ \mathrm{W\,m^{-2}\,K^{-1}}$. The +0.15 $\mathrm{W\,m^{-2}\,decade^{-1}}$ ERFaci sensitivity test is implemented by adding 0.15 $\mathrm{W\,m^{-2}\,decade^{-1}}$ to every draw of $\dot{F}$, without changing its uncertainty.

For the Monte Carlo calculation of $\mathcal{L}_N$, we draw plausible values T_j, F_j, and $\Delta\lambda_j$ of the true temperature trend, forcing trend, and $\Delta\lambda$, and define $\lambda_{dtj} = \lambda_{2\mathrm{xCO_2}} - \Delta\lambda_j$. Because the errors in $\dot{N}$ and $\dot{T}$ are correlated, the Gaussian density used to score N_o is conditioned on the corresponding temperature draw, although we find this covariance has a small effect on the resulting likelihoods. The mean and variance are

$$
\begin{aligned}
m_{N,j} &= F_j + \lambda_{dtj} T_j + \frac{c_{NT}}{\sigma_T^2}\left(T_o - T_j\right), \\
\sigma^2_{N|T} &= \sigma^2_N - \frac{c^2_{NT}}{\sigma^2_T}.
\end{aligned} \tag{20}
$$

The marginal likelihood is estimated as

$$
\mathcal{L}_N(\lambda_{2\mathrm{xCO_2}}) \approx \frac{1}{J}\sum_{j=1}^{J} \phi\left(N_o \mid m_{N,j}, \sigma_{N|T}\right), \tag{21}
$$

where $\phi(x \mid m, \sigma)$ denotes a Gaussian probability density with mean m and standard deviation σ. Thus, the subscript N identifies the direction in which the energy-budget residual is scored; $\mathcal{L}_N$ nevertheless uses information on observed trends in both N and T and accounts for their correlated uncertainty.

We calculate $\mathcal{L}_T$ analogously, but draw plausible values N_j, F_j, and $\Delta\lambda_j$ and score the observed temperature trend. In this case,

$$\begin{aligned}
m_{T,j} &= \frac{N_j - F_j}{\lambda_{dtj}} + \frac{c_{NT}}{\sigma_N^2}\left(N_o - N_j\right), \\
\sigma_{T|N}^2 &= \sigma_T^2 - \frac{c_{NT}^2}{\sigma_N^2},
\end{aligned} \tag{22}$$

and

$$\mathcal{L}_T(\lambda_{2\mathrm{xCO_2}}) \approx \frac{1}{J}\sum_{j=1}^{J} \phi\left(T_o \mid m_{T,j}, \sigma_{T|N}\right). \tag{23}$$

Because the uncertainty distributions are approximately Gaussian, the Monte Carlo calculations can also be checked semi-analytically (only semi-analytically because $\Delta\lambda$ requires numerical integration, but the λ-space calculation becomes fully analytic if $\Delta\lambda$ is ignored and λ_{dt} is inferred directly instead of $\lambda_{2\mathrm{xCO_2}}$.) After marginalizing over Gaussian uncertainty in $\dot{N}$, $\dot{T}$, and $\dot{F}$, the variance of the N-space residual is

$$V_N(\lambda_{dt}) = \sigma_N^2 + \sigma_F^2 + \lambda_{dt}^2\sigma_T^2 - 2\lambda_{dt}c_{NT}, \tag{24}$$

and its Gaussian density is

$$g_N(\lambda_{dt}) = \frac{1}{\sqrt{2\pi V_N(\lambda_{dt})}} \exp\left[-\frac{\left(N_o - \mu_F - \lambda_{dt}T_o\right)^2}{2V_N(\lambda_{dt})}\right]. \tag{25}$$

The corresponding T-space residual variance is

$$V_T(\lambda_{dt}) = \frac{V_N(\lambda_{dt})}{\lambda_{dt}^2}. \tag{26}$$

The two likelihoods are then

$$\begin{aligned}
\mathcal{L}_N(\lambda_{2\mathrm{xCO_2}}) &= \int g_N(\lambda_{2\mathrm{xCO_2}} - \Delta\lambda)\, p_{\Delta\lambda}(\Delta\lambda)\, \mathrm{d}\Delta\lambda, \\
\mathcal{L}_T(\lambda_{2\mathrm{xCO_2}}) &= \int \left|\lambda_{2\mathrm{xCO_2}} - \Delta\lambda\right| g_N(\lambda_{2\mathrm{xCO_2}} - \Delta\lambda)\, p_{\Delta\lambda}(\Delta\lambda)\, \mathrm{d}\Delta\lambda.
\end{aligned} \tag{27}$$

These expressions make the difference between the two likelihoods explicit: when the energy-budget residual is normalized as a Gaussian density in T space, it acquires the factor $|\lambda_{dt}| = |\lambda_{2xCO_2} - \Delta\lambda|$. Because $\Delta\lambda$ is uncertain, this factor remains inside the nuisance-parameter integral. It suppresses $\mathcal{L}_T$ as λ_{dt} approaches zero and gives greater relative weight to larger $|\lambda_{dt}|$. The remaining integral over $\Delta\lambda$ is evaluated numerically. The semi-analytic and Monte Carlo likelihoods agree within Monte Carlo sampling error, verifying that their differences arise from the statistical models rather than the numerical integration.

For inference in climate-sensitivity space,

$$F_{2xCO_2} \sim \mathcal{N}(\mu = 3.93, \sigma^2 = 0.29^2)\ \mathrm{W\,m^{-2}}, \tag{28}$$

and

$$\lambda_{2xCO_2} = -\frac{F_{2xCO_2}}{S}, \qquad \lambda_{dt} = -\frac{F_{2xCO_2}}{S} - \Delta\lambda. \tag{29}$$

For likelihoods of type k ($\mathcal{L}_k$, representing $\mathcal{L}_N$ or $\mathcal{L}_T$), define $w_N(\lambda_{dt}) = 1$ and $w_T(\lambda_{dt}) = |\lambda_{dt}|$. The likelihood for a fixed value of S is

$$\mathcal{L}_k(S) = \iint w_k(\lambda_{dt})\, g_N(\lambda_{dt})\, p_{\Delta\lambda}(\Delta\lambda)\, p_{F_{2xCO_2}}(F_{2xCO_2})\, \mathrm{d}\Delta\lambda\, \mathrm{d}F_{2xCO_2}. \tag{30}$$

No transformation Jacobian is required in Eq. (30) because S is held fixed while F_{2xCO_2} is marginalized as a nuisance quantity.

A Jacobian is required when transforming a prior specified in λ_{2xCO_2} into an S posterior:

$$\left|\frac{\partial \lambda_{2xCO_2}}{\partial S}\right| = \frac{|F_{2xCO_2}|}{S^2}. \tag{31}$$

The corresponding posterior is therefore

$$p_k(S \mid \mathbf{y}) \propto \iint w_k(\lambda_{dt})\, g_N(\lambda_{dt})\, p_{\Delta\lambda}(\Delta\lambda)\, p_{F_{2xCO_2}}(F_{2xCO_2})\, p_\lambda(-F_{2xCO_2}/S)\, \frac{|F_{2xCO_2}|}{S^2}\, \mathrm{d}\Delta\lambda\, \mathrm{d}F_{2xCO_2}. \tag{32}$$

The prior density and Jacobian remain inside the integral because the likelihood, prior transformation, and Jacobian depend on the same value of F_{2xCO_2}. We use the λ_{2xCO_2}

priors described in the main text and restrict the reported positive-S posteriors to $0.05 < S < 20$ K. We omit covariance between the CO_2 contribution to $\dot{F}$ and F_{2xCO_2}, which has been found to have a minor influence on historical likelihoods (Sherwood et al., 2020; Marvel & Webb, 2025).

Posterior PDFs are normalized by numerical integration. Medians and the 66% and 90% credible ranges correspond to the 50th, 17th–83rd, and 5th–95th percentiles, respectively. For the additional comparisons in Fig. S2, the profile likelihood (Lewis, 2023) maximizes the same joint Gaussian density over the nuisance quantities rather than integrating over them. The surface-integral method of Marvel and Webb (2025) instead integrates the joint evidence density over the energy-budget surface in $(\dot{T}, \dot{F}, \dot{N})$ space. With the Euclidean coordinate scaling, this introduces the geometric surface-area factor $\sqrt{(\lambda_{2xCO_2} - \Delta\lambda)^2 + 2}$. This factor depends on the relative scaling, and hence the units, assigned to the three coordinate axes. The profile and surface-integral likelihoods are included as methodological sensitivity tests; all primary posterior results use the marginal likelihood $\mathcal{L}_N$.

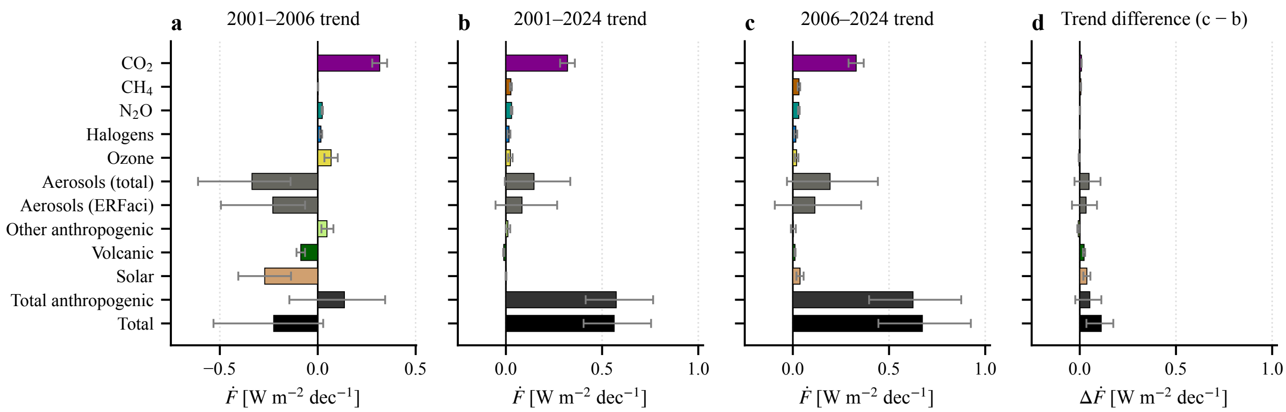

Figure S1. Trends in effective radiative forcing ($\dot{F}$) for various forcing components. Data is from the Indicators of Global Climate Change (IGCC) 100,000-member ensemble (Forster et al., 2025; Smith et al., 2025). Trends are shown for multiple periods, along with the difference between 2006–2024 and 2001–2024 trends in panel **d**. Errors are 90% ranges.

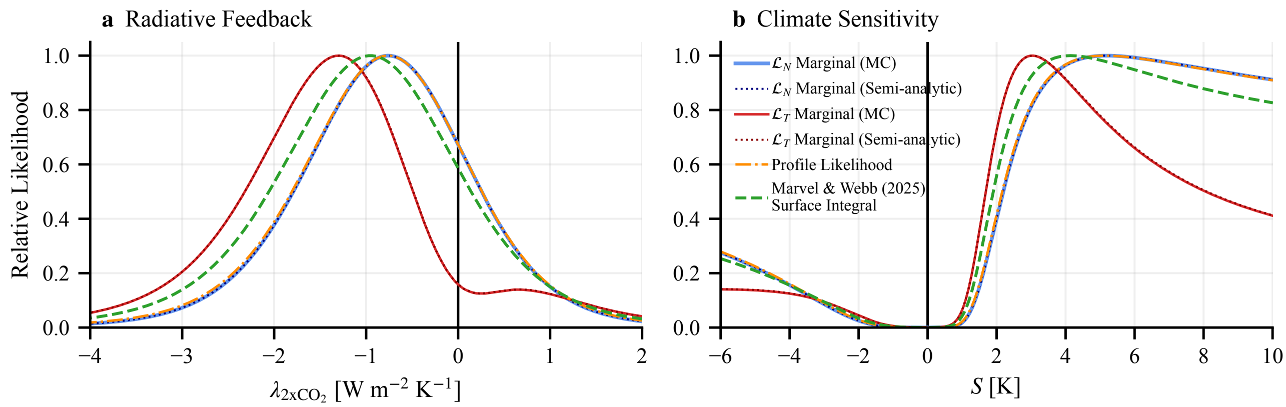

Figure S2. Comparison of likelihood-estimation methods in feedback (λ_{2xCO_2}) and climate-sensitivity (S) space. The preferred method proposed in this study, $\mathcal{L}_N$, evaluates the energy-budget residual in N space and marginalizes over uncertainty in T and the remaining nuisance quantities using Monte Carlo (MC) integration. The MC calculations agree with semi-analytic evaluations, which are only semi-analytic because they require numerical integration over $\Delta\lambda$. $\mathcal{L}_T$ follows the formulation used by Sherwood et al. (2020) and shown in the main text. Additional comparisons are the surface-integral method of Marvel and Webb (2025) and the profile likelihood, which is one of three equivalent methods considered by Lewis (2023). Profile and marginal likelihoods generally differ, although they can be proportional in special linear-Gaussian cases.

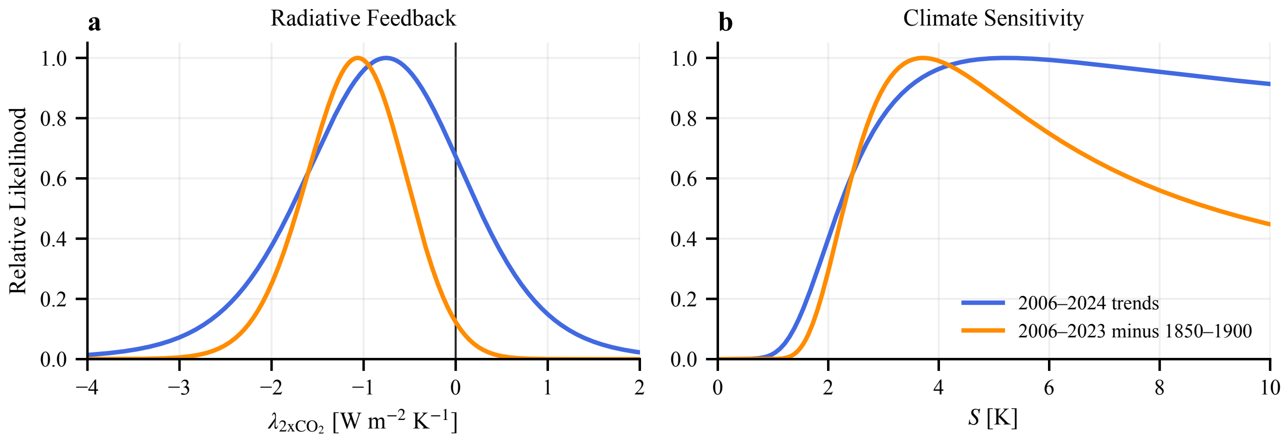

Figure S3. Comparison of likelihoods (as in main text Fig. 2) from the CERES-era trends over 2006–2024 in this study versus the historical record anomalies spanning 1850–2023. The historical record constraint is based on 2006–2023 mean anomalies relative to 1850–1900 from Cooper et al. (2026). Both likelihoods use the $\mathcal{L}_N$ approach.

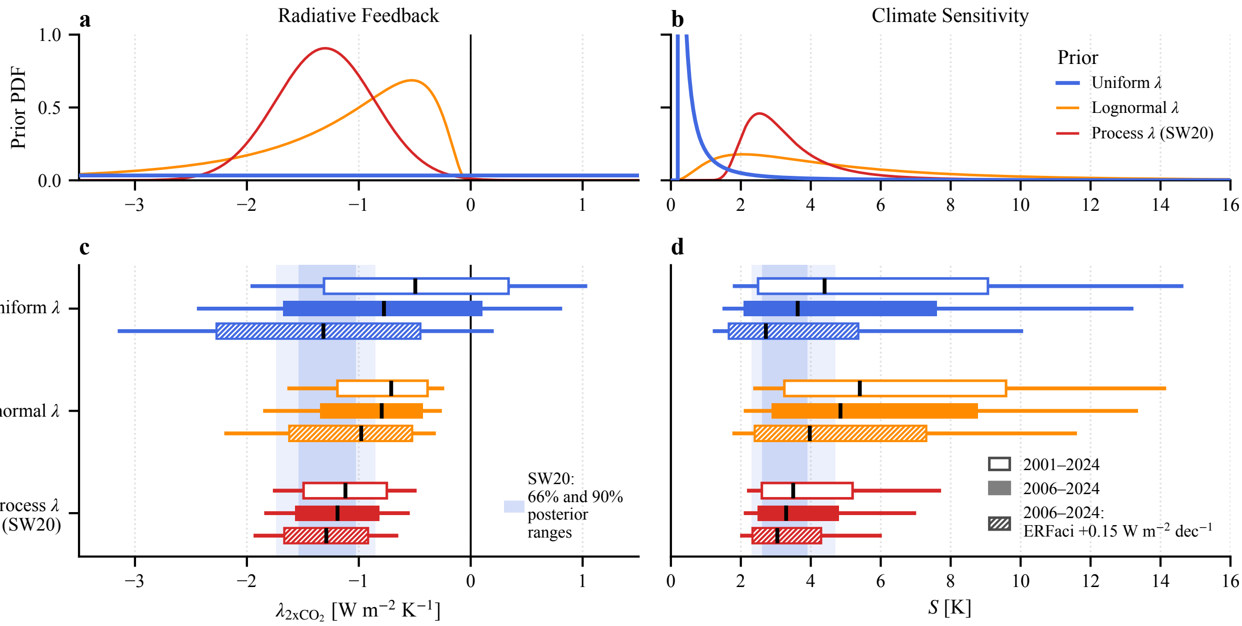

Figure S4. Posterior ranges including a test with ERFaci trends increased by 0.15 W m^{-2} dec^{-1}. As in main text Fig. 3, but including an additional posterior with an additional +0.15 W m^{-2} decade^{-1} added to all ERFaci trends. **(a–b)** Prior probability density functions (PDFs), which correspond to **(c–d)** posterior ranges.

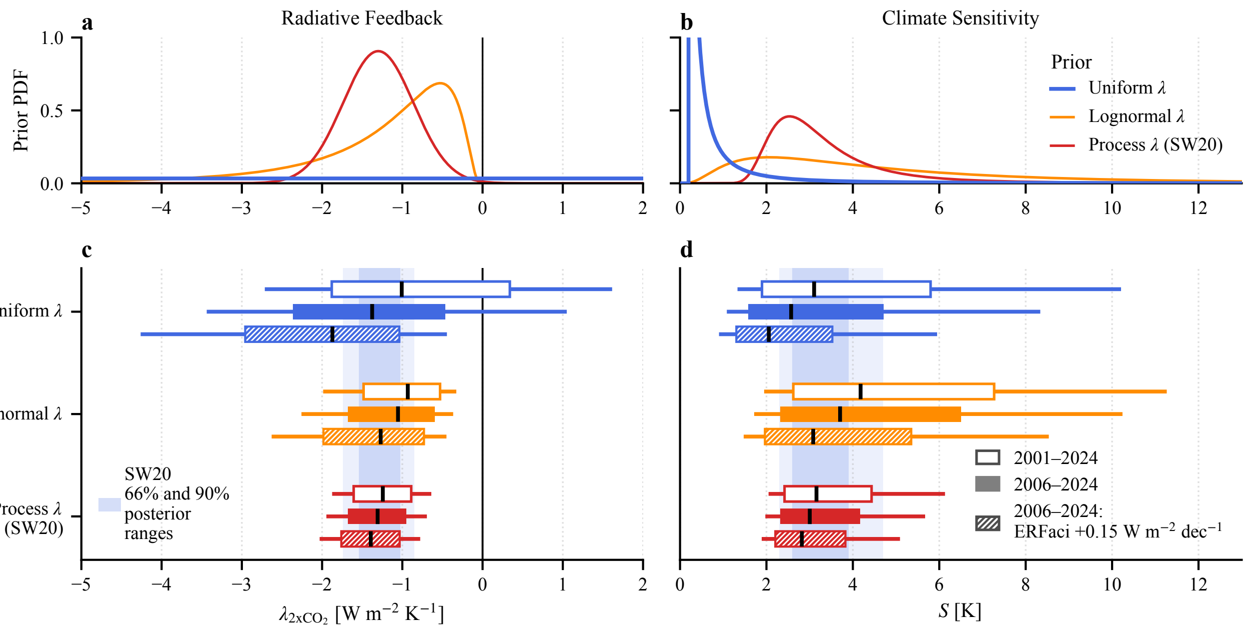

Figure S5. Posterior ranges using the $\mathcal{L}_T$ likelihood. (a–b) Prior probability density functions (PDFs), which correspond to **(c–d)** posterior ranges, as shown in Figs. 3 and S4, but using $\mathcal{L}_T$ instead of $\mathcal{L}_N$. Note the different horizontal axes compared to main text Figs. 3 and S4.

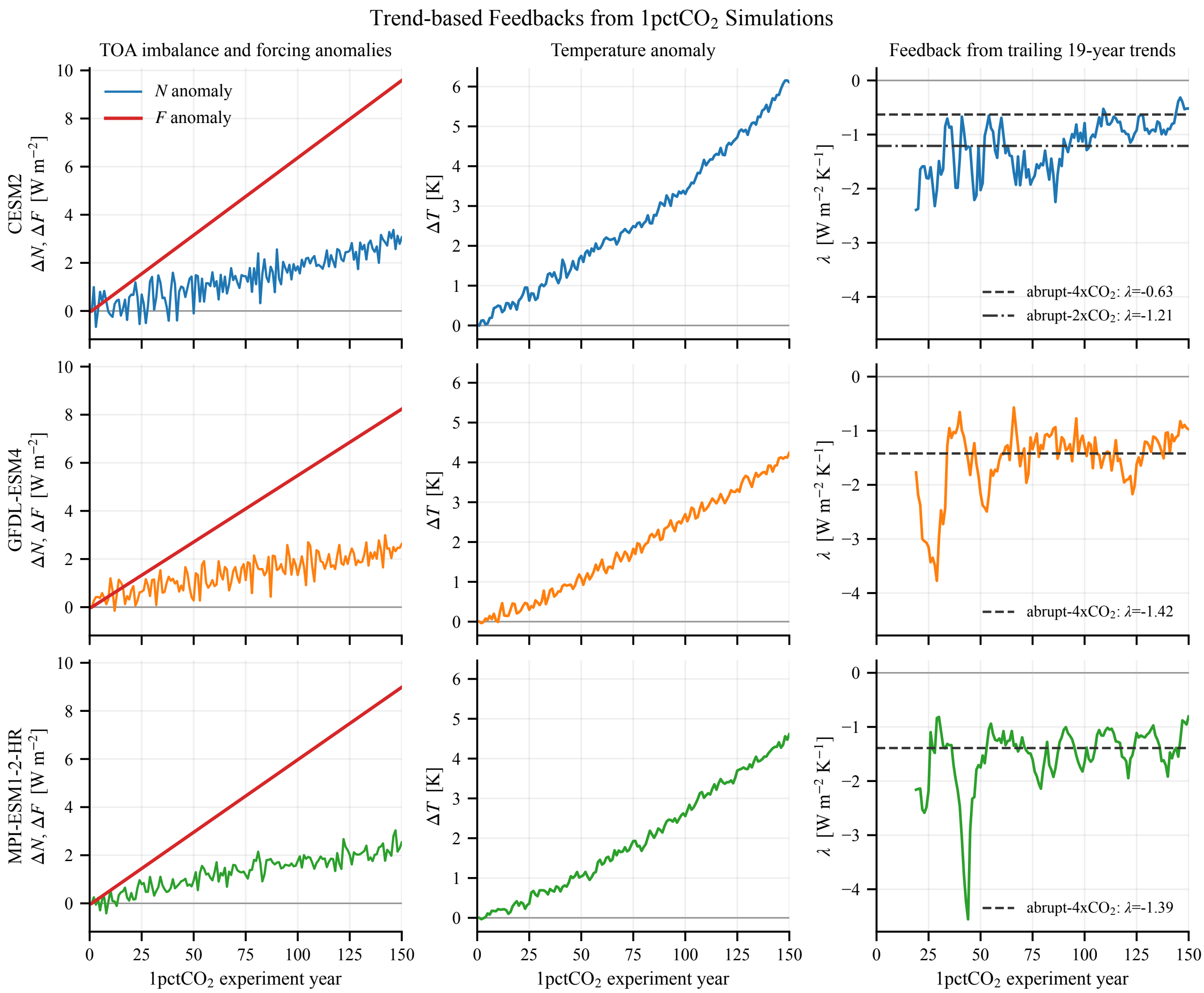

Figure S6. Trend-based feedbacks in 1pctCO$_2$ simulations. Model output is from CESM2 (Danabasoglu et al., 2020), GFDL-ESM4 (Dunne et al., 2020), and MPI-ESM1.2-HR (Mauritsen et al., 2019). Left and center columns show anomalies in TOA energy imbalance (N), effective radiative forcing (F), and global-mean near-surface air temperature (T). The right column shows feedbacks from trailing 19-year trends, $\lambda_{dt} = (\dot{N} - \dot{F})/\dot{T}$. Horizontal dashed lines show feedback estimates from abrupt-4xCO$_2$ simulations. Abrupt-2xCO$_2$ is also shown for CESM2; note Dvorak et al. (2025) find CESM2 $\lambda_{2\mathrm{xCO}_2} \approx -1.12\ \mathrm{W\,m^{-2}\,K^{-1}}$ in an extended simulation. CO$_2$ forcing is approximated as $F(t) = F_{2\mathrm{xCO}_2} \log[ppm(t)/ppm_0]/\log(2)$, where $ppm(t)/ppm_0 = 1.01^t$ and $F_{2\mathrm{xCO}_2}$ is the model-specific $F_{2\mathrm{xCO}_2}$ reported by Forster et al. (2021). Anomalies are shown relative to year one.

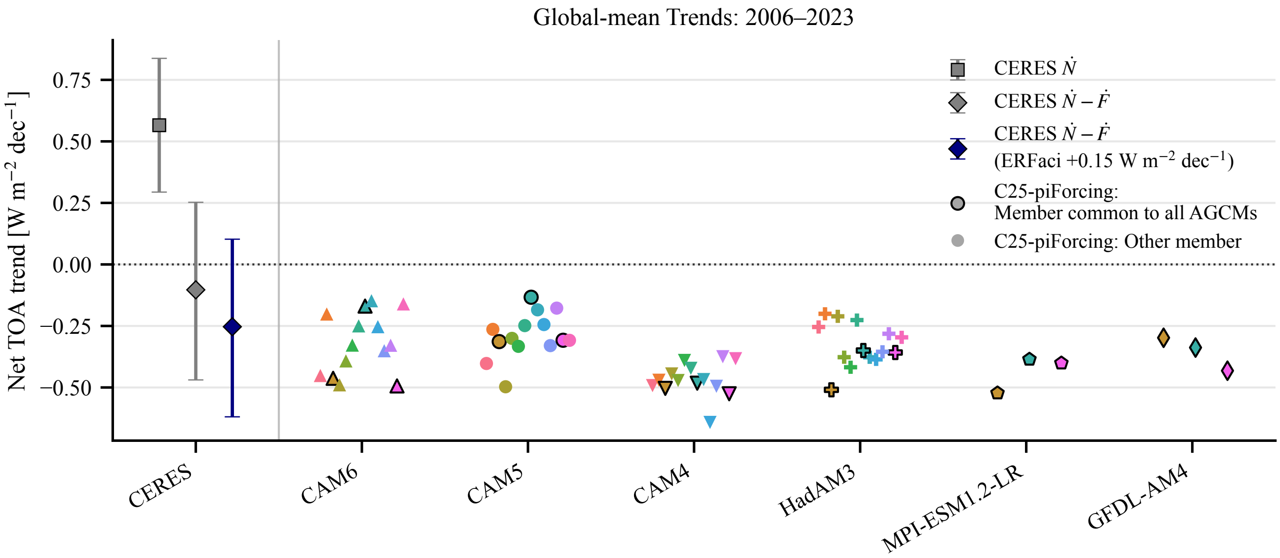

Figure S7. Net radiation trends at top-of-atmosphere (TOA) from CERES satellite data versus atmospheric general circulation models (AGCMs). CERES EBAF Ed4.2.1 trends in N (with trend denoted $\dot{N}$) from Loeb et al. (2018), showing the standard error from ordinary least squares (OLS) regression, and $\dot{N} - \dot{F}$ using the IGCC forcing ensemble (Forster et al., 2025; Smith et al., 2025). We also show $\dot{N} - \dot{F}$ with $+0.15$ W m^{-2} decade^{-1} added to $\dot{F}$, based on the forcing estimate for aerosol-cloud interactions (ERFaci) in Yuan et al. (2026). Errors are 90% ranges. C25-piForcing denotes AGCM simulations with constant preindustrial forcings in Cooper et al. (2026), which used SST and sea ice boundary conditions from an ensemble reconstruction (Cooper et al., 2025). Three of the boundary conditions were used in all six AGCMs, while four of the AGCMs used 14 boundary conditions; the boundary conditions are identified with consistent colors for each AGCM.

Table S1. Summary of input distributions, which are assumed to be Gaussian. "ERFaci" denotes the test with +0.15 $\mathrm{W\,m^{-2}\,decade^{-1}}$ added to $\dot{F}$. Units are $\mathrm{W\,m^{-2}\,decade^{-1}}$ for $\dot{N}$ and $\dot{F}$, $\mathrm{K\,dec^{-1}}$ for $\dot{T}$, $\mathrm{W\,m^{-2}\,K^{-1}}$ for $\Delta\lambda$, and $\mathrm{W\,m^{-2}}$ for F_{2xCO_2}. Lower panel reports the fixed $\dot{N}$–$\dot{T}$ covariance and correlation and the conditional σ used by the covariance-aware likelihoods. Covariance units are $\mathrm{K\,W\,m^{-2}\,dec^{-2}}$.

Analysis	Quantity	Mean	1σ	5%	95%
2001–2024	$\dot{N}$	0.45	0.10	0.28	0.62
2001–2024	$\dot{F}$	0.57	0.15	0.33	0.81
2001–2024	$\dot{T}$	0.24	0.06	0.15	0.34
2001–2024	$\Delta\lambda$	0.00	0.30	−0.49	0.49
2001–2024	F_{2xCO_2}	3.93	0.29	3.45	4.41
2006–2024	$\dot{N}$	0.45	0.16	0.19	0.72
2006–2024	$\dot{F}$	0.68	0.18	0.39	0.97
2006–2024	$\dot{T}$	0.30	0.07	0.18	0.41
2006–2024	$\Delta\lambda$	0.00	0.30	−0.49	0.50
2006–2024	F_{2xCO_2}	3.93	0.29	3.45	4.41
2006–2024 +ERFaci	$\dot{N}$	0.45	0.16	0.19	0.72
2006–2024 +ERFaci	$\dot{F}$	0.83	0.18	0.54	1.12
2006–2024 +ERFaci	$\dot{T}$	0.30	0.07	0.18	0.41
2006–2024 +ERFaci	$\Delta\lambda$	0.00	0.30	−0.49	0.49
2006–2024 +ERFaci	F_{2xCO_2}	3.93	0.29	3.45	4.41

Analysis	$\mathrm{Cov}(\dot{T},\dot{N})$	$\mathrm{Corr}(\dot{T},\dot{N})$	$\sigma_{\dot{N}\vert\dot{T}}$	$\sigma_{\dot{T}\vert\dot{N}}$
2001–2024	−0.0021	−0.35	0.10	0.05
2006–2024	−0.0030	−0.26	0.16	0.07
2006–2024 +ERFaci	−0.0030	−0.26	0.16	0.07

Table S2. Posterior summaries using the $\mathcal{L}_N$ likelihood. Columns labeled 5%–95% give posterior percentiles. "ERFaci" refers to the test using 2006–2024 with +0.15 $\mathrm{W\,m^{-2}\,decade^{-1}}$ added to the forcing trends to represent possible additional forcing from aerosol-cloud interactions. λ_{2xCO_2} is in $\mathrm{W\,m^{-2}\,K^{-1}}$ units, and S is in K.

Analysis	Prior	Parameter	Mean	Mode	5%	17%	50%	83%	95%
2001–2024	Uniform λ	λ_{2xCO_2}	−0.48	−0.51	−1.97	−1.31	−0.50	0.34	1.04
2001–2024	Lognormal λ	λ_{2xCO_2}	−0.79	−0.52	−1.64	−1.19	−0.71	−0.39	−0.24
2001–2024	SW20 process λ	λ_{2xCO_2}	−1.12	−1.12	−1.77	−1.49	−1.12	−0.75	−0.48
2006–2024	Uniform λ	λ_{2xCO_2}	−0.79	−0.76	−2.45	−1.68	−0.78	0.10	0.82
2006–2024	Lognormal λ	λ_{2xCO_2}	−0.89	−0.58	−1.85	−1.34	−0.80	−0.43	−0.26
2006–2024	SW20 process λ	λ_{2xCO_2}	−1.19	−1.19	−1.85	−1.57	−1.19	−0.81	−0.54
2006–2024 +ERFaci	Uniform λ	λ_{2xCO_2}	−1.38	−1.24	−3.15	−2.27	−1.32	−0.45	0.21
2006–2024 +ERFaci	Lognormal λ	λ_{2xCO_2}	−1.08	−0.74	−2.20	−1.62	−0.98	−0.52	−0.31
2006–2024 +ERFaci	SW20 process λ	λ_{2xCO_2}	−1.29	−1.29	−1.94	−1.67	−1.29	−0.92	−0.65
2001–2024	Uniform λ	S	5.7	2.7	1.8	2.5	4.4	9.1	14.7
2001–2024	Lognormal λ	S	6.4	3.7	2.4	3.2	5.4	9.6	14.2
2001–2024	SW20 process λ	S	4.0	2.9	2.2	2.6	3.5	5.2	7.7
2006–2024	Uniform λ	S	4.9	2.3	1.5	2.1	3.6	7.6	13.2
2006–2024	Lognormal λ	S	5.9	3.3	2.1	2.9	4.8	8.8	13.4
2006–2024	SW20 process λ	S	3.8	2.8	2.1	2.5	3.3	4.8	7.0
2006–2024 +ERFaci	Uniform λ	S	3.7	1.9	1.2	1.7	2.7	5.4	10.1
2006–2024 +ERFaci	Lognormal λ	S	4.9	2.7	1.8	2.4	4.0	7.3	11.6
2006–2024 +ERFaci	SW20 process λ	S	3.4	2.6	2.0	2.3	3.0	4.3	6.0

References

Cooper, V. T., Armour, K. C., Gregory, J. M., Andrews, T., Guenther, M., & Fan, C. (2026). *Historical Pattern Effects and Climate Sensitivity Revisited with Novel Constraints on Past Warming Patterns.* Retrieved from `https://eartharxiv.org/repository/view/14002/` doi: 10.31223/X5NF62

Cooper, V. T., Hakim, G. J., & Armour, K. C. (2025). Monthly Sea Surface Temperature, Sea Ice, and Sea Level Pressure over 1850–2023 from Coupled Data Assimilation. *Journal of Climate*, *38*(19), 5461–5490. Retrieved from `https://journals.ametsoc.org/view/journals/clim/38/19/JCLI-D-25-0021.1.xml` doi: 10.1175/JCLI-D-25-0021.1

Danabasoglu, G., Lamarque, J., Bacmeister, J., Bailey, D. A., DuVivier, A. K., Edwards, J., … Strand, W. G. (2020). The Community Earth System Model Version 2 (CESM2). *Journal of Advances in Modeling Earth Systems*, *12*(2). Retrieved from `https://onlinelibrary.wiley.com/doi/10.1029/2019MS001916` doi: 10.1029/2019MS001916

Dunne, J. P., Horowitz, L. W., Adcroft, A. J., Ginoux, P., Held, I. M., John, J. G., … Zhao, M. (2020). The GFDL Earth System Model Version 4.1 (GFDL-ESM 4.1): Overall Coupled Model Description and Simulation Characteristics. *Journal of Advances in Modeling Earth Systems*, *12*(11). Retrieved from `https://agupubs.onlinelibrary.wiley.com/doi/10.1029/2019MS002015` doi: 10.1029/2019MS002015

Dvorak, M., Armour, K. C., Feng, R., Cooper, V. T., Zhu, J., Burls, N., & Proistosescu, C. (2025). Mid-Pliocene Climate Forcing, Sea Surface Temperature Patterns, and Implications for Modern-Day Climate Sensitivity. *Journal of Climate*, *38*(13), 3037–3053. Retrieved from `https://journals.ametsoc.org/view/journals/clim/38/13/JCLI-D-24-0410.1.xml` doi: 10.1175/JCLI-D-24-0410.1

Forster, P., Storelvmo, T., Armour, K., Collins, W., Dufresne, J.-L., Frame, D., … Zhang, H.

(2021). The Earth's energy budget, climate feedbacks, and climate sensitivity. In V. Masson-Delmotte et al. (Eds.), *Climate change 2021: The physical science basis. contribution of working group i to the sixth assessment report of the intergovernmental panel on climate change* (chap. 7). Cambridge, UK and New York, NY: Cambridge University Press. doi: 10.1017/9781009157896.009

Forster, P. M., Smith, C., Walsh, T., Lamb, W. F., Lamboll, R., Cassou, C., … Zhai, P. (2025). Indicators of Global Climate Change 2024: annual update of key indicators of the state of the climate system and human influence. *Earth System Science Data*, *17*(6), 2641–2680. Retrieved from `https://essd.copernicus.org/articles/17/2641/2025/` doi: 10.5194/essd-17-2641-2025

Lewis, N. (2023). Objectively combining climate sensitivity evidence. *Climate Dynamics*, *60*(9-10), 3139–3165. Retrieved from `https://link.springer.com/10.1007/s00382-022-06468-x` doi: 10.1007/s00382-022-06468-x

Loeb, N. G., Doelling, D. R., Wang, H., Su, W., Nguyen, C., Corbett, J. G., … Kato, S. (2018). Clouds and the Earth's Radiant Energy System (CERES) Energy Balanced and Filled (EBAF) Top-of-Atmosphere (TOA) Edition-4.0 Data Product. *Journal of Climate*, *31*(2), 895–918. Retrieved from `https://journals.ametsoc.org/doi/10.1175/JCLI-D-17-0208.1` doi: 10.1175/JCLI-D-17-0208.1

Marvel, K., & Webb, M. (2025). Towards robust community assessments of the Earth's climate sensitivity. *Earth System Dynamics*, *16*(1), 317–332. Retrieved from `https://esd.copernicus.org/articles/16/317/2025/` doi: 10.5194/esd-16-317-2025

Mauritsen, T., Bader, J., Becker, T., Behrens, J., Bittner, M., Brokopf, R., … Roeckner, E. (2019). Developments in the MPI-M Earth System Model version 1.2 (MPI-ESM1.2) and Its Response to Increasing CO2. *Journal of Advances in Modeling Earth Systems*, *11*(4), 998–1038. Retrieved from https://agupubs.onlinelibrary.wiley.com/doi/10.1029/2018MS001400 doi: 10.1029/2018MS001400

Sherwood, S. C., Webb, M. J., Annan, J. D., Armour, K. C., Forster, P. M., Hargreaves, J. C., … Zelinka, M. D. (2020). An Assessment of Earth's Climate Sensitivity Using Multiple Lines of Evidence. *Reviews of Geophysics*, *58*(4). Retrieved from https://onlinelibrary.wiley.com/doi/10.1029/2019RG000678 doi: 10.1029/2019RG000678

Smith, C., Walsh, T., Gillett, N., Hauser, M., Krummel, P., Lamb, W., … Forster, P. (2025). Indicators of Global Climate Change 2024. *Zenodo*. Retrieved from https://doi.org/10.5281/zenodo.15744430 doi: 10.5281/zenodo.15744430

Yuan, T., Song, H., Kramer, R., Oreopoulos, L., Raghuraman, S. P., Wood, R., & Chin, M. (2026). Aerosol effective radiative forcing increases Earth's energy imbalance in recent decades. *Nature Communications*, *17*(1), 6322. Retrieved from https://www.nature.com/articles/s41467-026-72926-3 doi: 10.1038/s41467-026-72926-3